Fluid-structure interaction approximation with embedded solid-shell finite elements using discontinuous shape functions

A. Aguirre [a,b,] [iD], R. Zorrilla [a,c,] [iD], J. Baiges [a,c,*], R. Codina [a,c]

[a] *Universitat Politècnica de Catalunya, Jordi Girona 1-3, Edifici C1, Barcelona 08034, Spain*
[b] *Universidad de Santiago de Chile, Av. Libertador Bernardo O'Higgins 3363, Estación Central, Santiago, Chile*
[c] *International Center for Numerical Methods in Engineering (CIMNE), Spain*

ARTICLE INFO

ABSTRACT

This work introduces a numerical framework for addressing Fluid-Structure Interaction problems involving thin structures subject to finite strain deformations. The proposed approach utilizes an embedded mesh method to establish a coupling interface between the fluid and structural domains. The novelty of the work is the incorporation of a recently developed locking-free stabilized formulation of solid-shell elements to handle the structural domain. The framework employs established techniques to handle pressure jumps in the fluid domain across the embedding interface and enforce boundary conditions, such as discontinuous shape functions for the pressure unknowns designed to segregate nodal contributions of the cut elements, and Nitsche's method for the weak imposition of transmission conditions in the fluid. The present approach is validated through a series of benchmark cases in both 2D and 3D environments, progressively increasing in complexity. The results demonstrate good agreement with existing literature, establishing the presented framework as a viable method for addressing Fluid-Structure Interaction problems involving thin structures subject to large strains.

1. Introduction

The Fluid-Structure Interaction (FSI) problem is commonly formulated by solving the partial differential equations governing the fluid, structure, and the coupling conditions at the boundaries where the domains interact. Several families of numerical techniques exist to deal with this complex phenomenon, which need to define the strategy used to solve each of the components of the problem: the equations of fluid mechanics, the equations of solid mechanics, and the algorithmic approach for the coupling between both of them. This kind of problem can be approached by using either a monolithic or a partitioned scheme. The monolithic approach involves solving the fluid, structure, and interface equations as a unified system. Consequently, both domains advance simultaneously, requiring the solution of a large system of equations. On the other hand, the partitioned scheme employs separate solvers for each domain. Here, smaller independent systems of equations are solved separately, and the solution is obtained iteratively in a staggered manner. While the monolithic scheme results in a larger system of equations due to its simultaneous treatment of fluid, structure, and coupling equations, the partitioned approach involves solving smaller systems independently, coupling them iteratively. This efficiency makes the partitioned approach the preferred choice in many computational mechanics codes.

---

* Corresponding author.
E-mail addresses: alejandro.aguirre@upc.edu (A. Aguirre), rzorrilla@cimne.upc.edu (R. Zorrilla), joan.baiges@upc.edu (J. Baiges), ramon.codina@upc.edu (R. Codina).

However, the partitioned scheme has its drawbacks. Firstly, the coupling algorithm is not guaranteed to converge consistently [1]. Secondly, the added-mass instability arises when the density of the structure is comparable to or lower than that of the fluid. As implied by its name, this instability results in an added-mass effect or increased inertia of the structure due to the surrounding fluid not being able to occupy the same physical space simultaneously [2]. While the stability and convergence of the coupling process primarily depends on the ratio of the apparent added mass to the structural mass [3], the elasticity coefficients and time steps have to be taken into account to obtain stable solutions [4]. It is important to remark that the added-mass instability is not an inherent concern for all FSI problems. It rather becomes important in applications such as hemodynamics, where the blood as well as other biological tissues have similar densities [5–8], but is does not appear in cases where the density of the solid is greater than that of the fluid, such as in aeroelasticity problems [9–11]. Lastly, it is important to emphasize that the added-mass effect is not present in the monolithic approach, because the energy balance between fluid and structure is automatically satisfied [2].

In the context of partitioned schemes, coupling can be implemented using either a strong or a weak approach. Strong coupling schemes necessitate a sub-iteration algorithm involving both domains for each time step. Although this type of coupling is computationally expensive, it yields the same solution as the monolithic scheme after the iterative process. In contrast, weakly coupled schemes use the solution from one domain for each time step to subsequently solve the other domain in a staggered manner. However, this approach can introduce instabilities associated with the coupling procedure [12], including the added mass effect.

The numerical techniques to approach FSI problems can also be classified depending on whether or not fluid the mesh conforms to an interface between fluid and structure [13] and therefore, on how to communicate the information between the fluid, the solid and the mesh [10]. On the one hand, there are methods where the fluid mesh conforms to an interface; the most common approaches of this type are Arbitrary Lagrangian-Eulerian (ALE) methods [14] and deforming-spatial-domain or space-time procedures [15]. On the other hand, there are methods where the fluid and structure meshes do not conform; methods that follow this approach are the Embedded Mesh (EM) methods [16], where the embedded interface is implicitly represented by tools such as in cut-cell methods [17] and level-set methods [18]. It is important to note that, regardless of whether the mesh conforms to an interface, every FSI formulation requires the governing equations of both fields to satisfy the wall boundary conditions.

The ALE method considers a reference coordinate system for the fluid that moves accommodating the motion of the solid. While this method excels at accurately depicting sharp interfaces, it comes with the disadvantage of requiring adaptive meshes or re-meshing processes, which can be computationally expensive depending on the interface and the meshing algorithm [19]. In the FSI context, Navier-Stokes equations are written using an ALE description to accept moving boundaries, allowing the fluid to couple with Lagrangian solid elements [20,21].

Concerning EM methods, the solid and the fluid are discretized separately, and their meshes do not need to coincide at an interface. This flexibility allows the solid, described in a Lagrangian way, to move through the Eulerian-described fluid. Generally, EM methods can be classified into two types: Diffused Boundary Methods and Sharp Interface Methods [22]. In the former, the embedded boundaries are smeared by distributing the singular forces to the surrounding background mesh nodes. This family includes the classic Immersed Boundary (IB) method, first proposed by Peskin in [16], the Direct Forcing IB method [23], and the Penalization method [24]. The latter consist of methods that eliminate the smearing feature, such as Cut-Cell methods [25], Immersed Interface methods [26], Hybrid Cartesian-IB methods, and Curvilinear IB methods [27]. All these methods require imposing the boundary conditions in an unfitted manner. This is typically addressed by enforcing them in a weak sense. Techniques such as the penalty method [28], the Lagrange multipliers method [29], or the Nitsche method [30,31] are commonly utilized to handle this issue. EM methods are widely used in the literature in the FSI context. In [32] an IB method was used to induce vibrations of cylinders mounted in tandem through a fluid flow. In [33] gradient-based aerodynamic shape optimization was performed and applied to optimize aerodynamic designs. In [34] a combination of anisotropic mesh adaptation and a level-set method is used to model FSI problems with high definition on the embedded interface. Note that EM methods are not restricted to FEM approaches and FSI applications. There are several different implementations in the literature, developed for a variety of physics. In [35] an embedded method was used to simulate blast loadings in shell-like structures using high-order Finite Difference method. In [36] An IB method implemented in combination with the lattice Boltzmann method was used to solve FSI problems where the transmission conditions were communicated by a moving-least square method.

The approach used in this work corresponds to a EM method of the Cut Finite Element Method (Cut-FEM) type [37,38]. This family of methods allows to signal the exact position of the embedded interface by defining a iso-surface function to pinpoint its location. We prefer to adhere to Cut-FEM type approaches as they enable the attainment of accurate solutions through purely local boundary condition imposition [39]. A particular feature of our approach is that in elements intersected by the embedded interface, the conventional FE space is replaced by a discontinuous one. This substitution facilitates the disconnection of velocity and pressure fields in both sides of an intersected element, enabling the representation of solution discontinuities arising from the immersion of a thin body.

This study is a direct continuation of two previous works. The first one is dedicated to the analysis of numerical locking solid-shell elements and how to overcome it by using stabilized formulations [40], and the second one is dedicated to the extension of the stabilized formulation to finite strain theory [41]. The present work is dedicated to extend the concepts developed previously to the FSI problem by using an EM approach, wherein the solid mesh is embedded inside the fluid mesh. The main contribution of this work consists in the employment of the stabilized mixed displacement-stress formulations developed for solid-shell elements to handle FSI problems. For the present study, both domains are approached by using mixed formulations: in the fluid domain a velocity-pressure formulation, whereas in the solid domain a displacement-stress formulation. The use of mixed formulations is usually associated to an incompatibility in the space of the unknowns if not interpolated properly [42]. For that reason, the problem is approached by means of stabilized formulations. The stabilization techniques are based on the VMS framework, which enables the use of equal-order

interpolation for unknowns and, in the case of the solid-shell elements, it also ensures that the formulation is free from the numerical locking that is inherent to them.

In addition to the stabilized Finite Element (FE) formulations utilized for solving each individual problem, the present FSI approach requires several essential components to be achieved properly. Firstly, it is necessary to implement a search algorithm to find the intersection of the solid interface inside the fluid elements, ensuring the accurate definition of the intersection and the new integration points. This task is non-trivial, as search algorithms can be computationally costly if not implemented efficiently. Secondly, there is a need to define shape functions capable of handling pressure-segregated domains. Thirdly, a proper strategy must be chosen to impose the transmission conditions at the interfaces of the solid and the fluid. Lastly, in strongly coupled schemes, it is crucial to ensure the convergence of the transmission conditions. Therefore, a coupling strategy is required to minimize the interface residuals. All of these challenges are thoroughly addressed in the present work.

This work is organized as follows: the geometrical approximation of the shell domain is briefly explained in Section 2. It is followed by the introduction of the governing equations of the fluid and solid problems in Section 3, where the solid dynamics equations in finite strain theory and Navier-Stokes continuum equations are summarized, starting with the differential form of the corresponding boundary value problems in Subsection 3.1. The variational form of the solid and fluid problems are explained in Subsection 3.2, presented in their mixed displacement-stress and velocity-pressure formulations, respectively. The time integration and linearization are described in Section 4. Consecutively, the stabilization techniques are briefly summarized in Section 5. Then, a brief summary of the construction of discontinuous shape functions is presented in Section 6. Details regarding the FSI problem, including the transmission conditions and the coupling strategy, are explained in Section 7. Some numerical examples are portrayed in Section 8. Lastly, the final remarks and conclusions are presented in Section 9.

2. Geometrical approximation of solid-shells using finite elements

2.1. Construction of the local basis

Let us summarize the construction of the geometrical approximation to solid-shells presented in [40]. Let us first consider the shell as a surface, represented by Ω_s^{2D} in $\mathbb{R}^3$. Suppose that we have a FE partition $\mathcal{T}_h = \{K\}$ of Ω_s^{2D} of diameter h, so that $\bar{\Omega}^{2D} = \bigcup_{K \in \mathcal{T}_h} K$. Let $K \in \mathcal{T}_h$ be an element domain of the partition with isoparametric coordinates (ξ, η), its mapping from the reference domain $K_0 \subset \mathbb{R}^2$ to $K \subset \mathbb{R}^3$ defined as

$$\boldsymbol{\varphi}_K : K_0 \longrightarrow K$$
$$(\xi, \eta) \mapsto (x^1, x^2, x^3). \tag{2.1}$$

Consider n_{nod} as the number of nodes of K, and a Lagrangian interpolation

$$\boldsymbol{\varphi}_K(\xi, \eta) = \sum_{A=1}^{n_{\text{nod}}} N^A(\xi, \eta) \boldsymbol{x}^A, \tag{2.2}$$

where $N^A(\xi, \eta)$ is the shape function of node A on K_0, and $\boldsymbol{x}^A$ is the position vector of node A in K, $A = 1, \ldots, n_{\text{nod}}$. The collection of all mappings $\{\boldsymbol{\varphi}_K, K \in \mathcal{T}_h\}$ provides a local parametrization of Ω_s^{2D}. The vectors tangent to each $K \in \mathcal{T}_h$ can be constructed as

$$\boldsymbol{g}_{1,K}^* = \left| \frac{\partial \boldsymbol{\varphi}_K}{\partial \xi} \right|^{-1} \frac{\partial \boldsymbol{\varphi}_K}{\partial \xi}, \quad \frac{\partial \boldsymbol{\varphi}_K}{\partial \xi} = \sum_{A=1}^{n_{\text{nod}}} \frac{\partial N^A}{\partial \xi} \boldsymbol{x}^A, \tag{2.3}$$

$$\boldsymbol{g}_{2,K}^* = \left| \frac{\partial \boldsymbol{\varphi}_K}{\partial \eta} \right|^{-1} \frac{\partial \boldsymbol{\varphi}_K}{\partial \eta}, \quad \frac{\partial \boldsymbol{\varphi}_K}{\partial \eta} = \sum_{A=1}^{n_{\text{nod}}} \frac{\partial N^A}{\partial \eta} \boldsymbol{x}^A, \tag{2.4}$$

which allow us to compute vectors normal to each $K \subset \Omega_s^{2D}$ as

$$\boldsymbol{g}_{3,K}^* = \boldsymbol{g}_{1,K}^* \times \boldsymbol{g}_{2,K}^*. \tag{2.5}$$

If ξ and η are orthogonal coordinates, $|\boldsymbol{g}_{3,K}^*| = 1$; otherwise, $\boldsymbol{g}_{3,K}^*$ is normalized.

The basis vectors $\{\boldsymbol{g}_{1,K}^*, \boldsymbol{g}_{2,K}^*, \boldsymbol{g}_{3,K}^*\}$, are discontinuous across elements if they are computed in this manner. However, they can be used to obtain a continuous basis. First, we project the vector field $\boldsymbol{g}_{3,K}^*$, $K \in \mathcal{T}_h$, onto the space of continuous vector fields using a standard $L^2(\Omega_s^{2D})$ projection, thus obtaining the nodal vectors $\boldsymbol{g}_3^a$, $a = 1, \ldots, n_{\text{pts}}$, for the nodal points n_{pts} of $\mathcal{T}_h$. Then it follows that

$$\boldsymbol{g}_3(x^1, x^2, x^3) = \frac{\sum_{a=1}^{n_{\text{pts}}} N^a(x^1, x^2, x^3) \boldsymbol{g}_3^a}{\left| \sum_{a=1}^{n_{\text{pts}}} N^a(x^1, x^2, x^3) \boldsymbol{g}_3^a \right|},$$

where N^a is the global shape function of node a. Within each element $K \in \mathcal{T}_h$ we have

$$\boldsymbol{g}_3|_K(\xi, \eta) = \frac{\sum_{A=1}^{n_{\text{nod}}} N^A(\xi, \eta) \boldsymbol{g}_{3,K}^A}{\left| \sum_{A=1}^{n_{\text{nod}}} N^A(\xi, \eta) \boldsymbol{g}_{3,K}^A \right|} \tag{2.6}$$
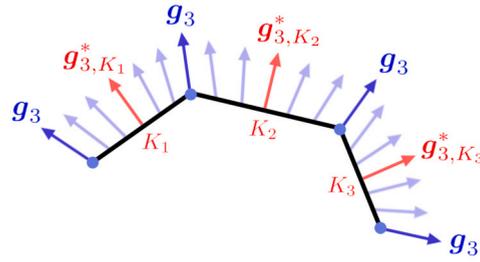
Fig. 1. Normal vectors to the shell $g^*_{3,K}$ and their smoothing g_3.
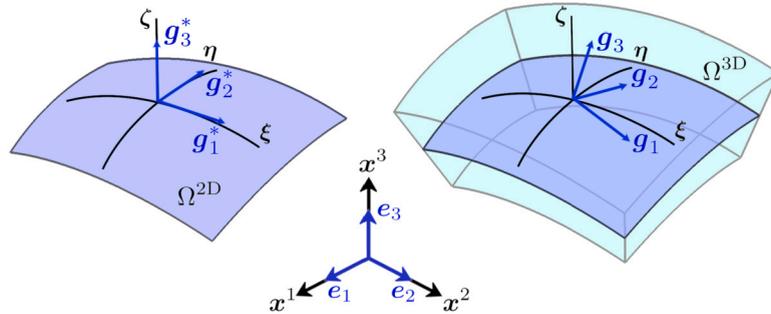

Fig. 2. Geometry of the shell: 2D surface (left) and 3D extruded volume (right).

where A is the local numbering of the global node a. Fig. 1 shows a cut of a surface and the conceptual difference between $g^*_{3,K}$ and g_3. Note that for linear elements $g^*_{3,K}$ will be constant on each $K \in \mathcal{T}_h$.

Let $\{e_1, e_2, e_3\}$ be the canonical basis of $\mathbb{R}^3$. Once the continuous global vector field g_3 is constructed, a continuous local basis can be built at each point $\{g_1, g_2, g_3\}$ by defining

$$g_1 = \frac{g_3 \times e_3}{|g_3 \times e_3|} \tag{2.7}$$

$$g_2 = g_3 \times g_1, \tag{2.8}$$

the only exception being when g_3 aligns with e_3, case in which we set $g_1 = e_1$ and $g_2 = e_2$ or $g_1 = -e_1$ and $g_2 = -e_2$ if g_3 is opposite to e_3. The covariant basis $\{g_1, g_2, g_3\}$ constructed this way will be such that $\{g_1, g_2\}$ will be *approximately* tangent to Ω_s^{2D} and g_3 *approximately* normal.

2.2. Extrusion of the shell mid-surface

The solid-shell domain where the calculations are performed is denoted as Ω_s^{3D}, and it is computed from the normal direction extrusion of Ω_s^{2D}, which also represents the mid-surface of the shell. The construction of Ω_s^{3D} can be done element-wise due to the continuity of g_3.

Consider the thickness of the shell to be defined by its values at the nodes of $\mathcal{T}_h$, denoted as t^a, $a = 1, \ldots n_{\text{pts}}$. For each $K \in \mathcal{T}_h$, the thicknesses at the nodes will be t_K^A, A being the local number of node a, and the thickness function can be constructed as

$$t_K(\xi, \eta) = \sum_{A=1}^{n_{\text{nod}}} N^A(\xi, \eta) t_K^A. \tag{2.9}$$

The 3D element $K_0^{3D} = K_0 \times [-1, 1]$ can be constructed from the reference element K_0, and the mapping

$$\psi_K : K_0^{3D} \longrightarrow \mathbb{R}^3$$

$$(\xi, \eta, \zeta) \mapsto (x^1, x^2, x^3) = \varphi_K(\xi, \eta) + \zeta \frac{1}{2} t_K(\xi, \eta) g_3|_K(\xi, \eta), \tag{2.10}$$

and then set $K^{3D} = \psi_K(K_0^{3D})$, i.e., the image of K_0^{3D} through ψ_K. The solid domain where the problem is posed is then $\Omega_s^{3D} = \bigcup_{K \in \mathcal{T}_h} K^{3D}$. From the continuity of g_3 and the intrinsic continuity of the thickness function, Ω_s^{3D} will be a smooth extrusion of Ω_s^{2D}. This domain is depicted in Fig. 2.

2.3. Interpolation across the thickness

After constructing the element domain $\{K^{3D}\}$, it only remains to define their degrees of freedom and basis for the FE space. Let us consider continuous Lagrangian interpolations for the original partition $\{K\}$ to define them for the reference element $K_0 \times [-1, 1]$. Let $N_i^{A,A'}(\xi, \eta, \zeta)$ be the shape function of a node in $K_0 \times [-1, 1]$ that corresponds to node A of K_0 and node A' of the discretization of $[-1, 1]$. The shape functions corresponding to the solid-shell body $N_i^{A,A'}(\xi, \eta, \zeta)$ are constructed by multiplying the mid-surface shape functions $N^A(\xi, \eta)$ and the standard one dimensional Lagrangian shape functions $N^{A'}(\zeta)$ in the isoparametric space as

$$N^{A,A'}(\xi, \eta, \zeta) = N^A(\xi, \eta)\, N^{A'}(\zeta). \tag{2.11}$$

At the global level the shape functions will be written as $N^a(x^1, x^2, x^3)$, with a running again from 1 to n_{pts}. The FE partition resulting from the extrusion of the FE partition of the shell surface $\mathcal{T}_h = \{K\}$ will be denoted as $\mathcal{T}_h^{3D} = \{K^{3D}\}$. From this point forward, the superscript 3D will be omitted for simplicity, since the following formulations as well as the numerical experiments are presented by considering the 3D approximation of the shell.

3. Governing equations

3.1. Boundary value problems

3.1.1. Finite strain solid continuum equations

Consider the solid domain to be $\Omega_s(t)$ of $\mathbb{R}^d$ at the current time $t \geq 0$, where $d \in \{2, 3\}$ is the number of space dimensions; consequently $\Omega_s(t)$ is the current configuration and $\Gamma_s(t) = \partial\Omega_s(t)$ is the domain boundary at time t. The domain and its boundary defined in the reference configuration are denoted by $\Omega_s^0 = \Omega_s(0)$ and $\Gamma_s^0 = \partial\Omega_s^0$, respectively. Let us consider the motion $\boldsymbol{\phi}$ of the deformable solid through a time interval $]0, T[$, whose mapping is described by $\boldsymbol{\phi} : \Omega_s^0 \to \Omega_s(t)$. The solid particles are labeled $\boldsymbol{X} \in \Omega_s^0$ and $\boldsymbol{x} \in \Omega_s(t)$ for the initial and current configurations, respectively, and the motion is defined as

$$\boldsymbol{x} = \boldsymbol{\phi}(\boldsymbol{X}, t). \tag{3.1}$$

Consider the space-time domain $\boldsymbol{D} = \{(\boldsymbol{X}, t) \mid \boldsymbol{X} \in \Omega_0, t \in]0, T[\}$ where the problem is defined. This problem consists of finding a displacement field $\boldsymbol{u}_s : \boldsymbol{D} \to \mathbb{R}^d$ and a second Piola-Kirchhoff (PK2) stress tensor field $\boldsymbol{S}_s : \boldsymbol{D} \to \mathbb{R}^d \otimes \mathbb{R}^d$ such that

$$\rho_s^0 \frac{\partial^2 u_{s_a}}{\partial t^2} - \frac{\partial}{\partial X_A}\{F_{s_{aB}} S_{s_{BA}}\} = \rho_s^0 b_{s_a} \qquad \text{in } \Omega_s^0, t \in]0, T[, \tag{3.2}$$

$$S_{s_{AB}} - 2\frac{\partial \Psi_s}{\partial C_{s_{AB}}} = 0 \qquad \text{in } \Omega_s^0, t \in]0, T[, \tag{3.3}$$

$$\rho_s J_s = \rho_s^0 \qquad \text{in } \Omega_s^0, t \in]0, T[, \tag{3.4}$$

$$\boldsymbol{u}_s = \boldsymbol{u}_{s,D} \qquad \text{on } \Gamma_{s,D}^0, t \in]0, T[, \tag{3.5}$$

$$\boldsymbol{n}_s \cdot \boldsymbol{\sigma}_s = \boldsymbol{t}_{s,N} \qquad \text{on } \Gamma_{s,N}^0, t \in]0, T[, \tag{3.6}$$

$$\boldsymbol{u}_s = \boldsymbol{u}_s^0 \qquad \text{in } \Omega_s^0, t = 0, \tag{3.7}$$

$$\dot{\boldsymbol{u}}_s = \dot{\boldsymbol{u}}_s^0 \qquad \text{in } \Omega_s^0, t = 0. \tag{3.8}$$

For clarity, we have used index notation in (3.2)-(3.3), with index a (in the deformed configuration) and A, B, C, D (in the reference configuration) running from 1 to d, and using the summation convention. Note that in Eq. (3.6) $\boldsymbol{\sigma}_s$ is the Cauchy stress tensor for the solid, which is related to PK2 by $\boldsymbol{\sigma}_s = \boldsymbol{F}_s \cdot \boldsymbol{S}_s$. This tensor is referred to the deformed configuration and can be expressed either in terms of $\boldsymbol{X}$ when using the Lagrangian description or in terms of $\boldsymbol{x}$ when using the Eulerian one. When imposing equilibrium of normal stresses in the solid and the fluid (see Eq. (7.2) below) this equilibrium will hold at each spatial point $\boldsymbol{x}$.

Let us briefly discuss the above equations. Eq. (3.2) is the balance of linear momentum equation in a total Lagrangian framework, where $\boldsymbol{F}_s = \frac{\partial \boldsymbol{x}}{\partial \boldsymbol{X}}$ is the deformation gradient, ρ_s is the density at time t, ρ_s^0 is the initial density, $J_s = \det(\boldsymbol{F}_s) > 0$ is the determinant of the deformation gradient, $\boldsymbol{S}_s$ is the second Piola-Kirchhoff (PK2) stress tensor whose symmetry is implied by the angular momentum equations, and $\rho_s^0 \boldsymbol{b}$ are the body forces. Eq. (3.3) correspond to the constitutive equation, where the PK2 stress tensor is written in terms of the strain energy function Ψ_s by taking derivatives with respect to the right Cauchy-Green tensor $\boldsymbol{C}_s = \boldsymbol{F}_s^T \cdot \boldsymbol{F}_s$. Eq. (3.4) is the mass conservation equation, Eq. (3.5) is the imposition of displacement boundary conditions $\boldsymbol{u}_{s,D}$ on the Dirichlet boundaries, Eq. (3.6) is the imposition of prescribed tractions $\boldsymbol{t}_N$ on the Neumann boundaries $\Gamma_{s,N}^0$ considering the outward unit vector $\boldsymbol{n}_s$ normal to the reference configuration boundary, and Eqs. (3.7)-(3.8) are the imposition of initial displacements $\boldsymbol{u}_s^0$ and velocities $\dot{\boldsymbol{u}}_{s,0} = \frac{\partial \boldsymbol{u}_s}{\partial t}\big|_{t=0}$, respectively.

The material is considered as a non-linear isotropic hyperelastic model. Therefore, Ψ_s is built as a function of the invariants of $\boldsymbol{C}_s$, defined as

$$I_1 = \text{trace}(\boldsymbol{C}_s) = \boldsymbol{C}_s : \boldsymbol{I},$$

$$I_2 = \text{trace}(\boldsymbol{C}_s \cdot \boldsymbol{C}_s) = \boldsymbol{C}_s : \boldsymbol{C}_s,$$

$$I_3 = \det(\boldsymbol{C}_s) = J_s^2.$$

The compressible Neo-Hookean material stored energy function is defined in terms of the invariants as

$$\Psi_s = \frac{\mu_s}{2}\left(I_1 - 3\right) - \mu_s \ln J_s + \frac{\lambda_s}{2}\left(\ln J_s\right)^2 \tag{3.9}$$

where μ_s and λ_s are Lamé material coefficients. Therefore, Ψ_s measures the work done by stresses from the initial to the current configuration, making the relationship between Ψ_s and $\boldsymbol{C}_s$ to be independent of the coordinate system chosen. Note that in a rigid body motion, or absence of deformation, the deformation gradient is the identity and the stored energy function vanishes. For this specific material, an expression for the PK2 stress tensor can be obtained from Eq. (3.3), resulting in

$$\boldsymbol{S}_s = \mu_s\left(\boldsymbol{I} - \boldsymbol{C}_s^{-1}\right) + \lambda_s\left(\ln J_s\right)\boldsymbol{C}_s^{-1}. \tag{3.10}$$

The solid mechanics problem is presented through a mixed displacement-PK2 stress formulation. The reason lies in the fact that the interpolation of $\boldsymbol{S}_s$ allows to overcome numerical locking inherent to shell problems, as has been proven in previous works [40,41]. The finite strain formulation has already been developed in [41], and therefore in the present work it is only briefly recalled for completeness. It is also worth mentioning that the extension to incompressible materials can be achieved by adopting a decoupled representation of the strain energy function which divides it into the deviatoric and volumetric parts [43,44].

3.1.2. Navier-Stokes continuum equations

Let us consider a computational domain Ω_f of $\mathbb{R}^d$ for dimensions $d \in \{2,3\}$, with boundaries Γ_f, in a time interval $]0,T[$. The standard two-field Navier-Stokes problem for incompressible fluid consists in finding the velocity $\boldsymbol{u}_f$ and pressure p_f such that

$$\rho_f \frac{\partial \boldsymbol{u}_f}{\partial t} + \rho_f \boldsymbol{u}_f \cdot \nabla \boldsymbol{u}_f - \nabla \cdot \left(2\mu_f \nabla^s \boldsymbol{u}_f\right) + \nabla p_f = \boldsymbol{f}_f \qquad \text{in } \Omega_f(t), t \in]0,T[, \tag{3.11}$$

$$\nabla \cdot \boldsymbol{u}_f = 0 \qquad \text{in } \Omega_f(t), t \in]0,T[, \tag{3.12}$$

$$\boldsymbol{u}_f = \boldsymbol{u}_{f,D} \qquad \text{on } \Gamma_{f,D}(t), t \in]0,T[, \tag{3.13}$$

$$\boldsymbol{n}_f \cdot \boldsymbol{\sigma}_f = \boldsymbol{t}_{f,N} \qquad \text{on } \Gamma_{f,N}(t), t \in]0,T[, \tag{3.14}$$

$$\boldsymbol{u}_f = \boldsymbol{u}_{f,0} \qquad \text{in } \Omega_f(t), t = 0, \tag{3.15}$$

where Eqs. (3.11)-(3.12) are the balance of linear momentum and the incompressibility restraint, respectively, Eqs. (3.13)-(3.14) are the Dirichlet and Neumann boundary conditions, and Eq. (3.15) is the velocity initial condition. In the balance of linear momentum equation, ρ_f is the fluid density, μ_f is the dynamic Newtonian viscosity, $\nabla^s \boldsymbol{u}_f = \frac{1}{2}\left(\nabla \boldsymbol{u}_f + \left(\nabla \boldsymbol{u}_f\right)^T\right)$ is the symmetrical gradient of the velocity vector, and $\boldsymbol{f}_f$ is the body forces vector. In the boundary condition equations, $\boldsymbol{u}_{f,D}$ is the prescribed velocity in the Dirichlet boundary, $\boldsymbol{n}_f$ is the unit normal pointing outwards from the fluid in the interface, $\boldsymbol{\sigma}_f = -p\boldsymbol{I} + 2\mu_f \nabla^s \boldsymbol{u}_f$ is the Cauchy stress tensor, and $\boldsymbol{t}_{f,N}$ is the prescribed fluid traction on the Neumann boundaries. Lastly, the initial velocity condition $\boldsymbol{u}_{f,0}$ is given to supply the governing equations.

3.2. Variational form

Let us consider $H^1(\Omega)$ to be the space of $L^2(\Omega)$ functions whose derivatives belong to $L^2(\Omega)$, for a domain Ω. In a general manner, the integral of the product of two functions in a domain ω is denoted by $\langle \cdot, \cdot \rangle_\omega$, omitting the subscript when ω is either Ω_s^0 or Ω_f depending on the problem being referred to. The variational form of the solid or fluid flow problems are defined in the following.

3.2.1. Variational form for the solid problem

For the solid problem the spaces are defined as $\mathbb{U} \subset H^1(\Omega_s)^d$ and $\mathbb{T} \subset L^2(\Omega_s)^{d \times d}$ for the displacements and the PK2 stresses, respectively, for all time $t \in]0,T[$. Functions in $\mathbb{U}$ satisfy the Dirichlet boundary conditions, whereas we denote as $\mathbb{U}_0$ the space of functions that vanish on the Dirichlet boundary of the solid domain $\Gamma_{s,D}^0$. Let $\mathbb{W} = \mathbb{U} \times \mathbb{T}$ and $\mathbb{W}_0 = \mathbb{U}_0 \times \mathbb{T}$ be the spaces where the weak form of the solid problem is defined, so that the unknowns $\boldsymbol{U}_s = \left[\boldsymbol{u}_s, \boldsymbol{S}_s\right]^T$ and test functions $\boldsymbol{V}_s = \left[\boldsymbol{v}_s, \boldsymbol{T}_s\right]^T$ are such that $\boldsymbol{U}_s \in \mathbb{W}$ for each time t and $\boldsymbol{V}_s \in \mathbb{W}_0$, respectively. By testing system (3.2)-(3.3) against arbitrary test functions $\boldsymbol{V}_s$, the weak form of the problem consists of finding $\boldsymbol{U}_s :]0,T[\mapsto \mathbb{W}$ such that the initial conditions are satisfied and

$$\left\langle \boldsymbol{v}_s, \rho_s^0 \frac{\partial^2 \boldsymbol{u}_s}{\partial t^2} \right\rangle + \mathcal{A}_s\left(\boldsymbol{V}_s, \boldsymbol{U}_s\right) = \mathcal{F}_s\left(\boldsymbol{V}_s\right) \quad \forall \boldsymbol{V}_s \in \mathbb{W}_0, \tag{3.16}$$

where $\mathcal{A}_s(\boldsymbol{V}_s, \boldsymbol{U}_s)$ is a semilinear form defined on $\mathbb{W}_0 \times \mathbb{W}$ as

$$\mathcal{A}_s(\boldsymbol{V}_s, \boldsymbol{U}_s) := \left\langle \frac{\partial v_{s_a}}{\partial X_A}, F_{s_{aB}} S_{s_{AB}} \right\rangle + \left\langle T_{s_{AB}}, S_{s_{AB}} \right\rangle - \left\langle T_{s_{AB}}, 2\frac{\partial \Psi_s}{\partial C_{s_{AB}}} \right\rangle, \tag{3.17}$$

and $\mathcal{F}_s(\boldsymbol{V}_s)$ is a linear form on $\mathbb{W}_0$ defined by

$$\mathcal{F}_s(\boldsymbol{V}_s) := \left\langle \boldsymbol{v}_s, \rho_s^0 \boldsymbol{b} \right\rangle + \left\langle \boldsymbol{v}_s, \boldsymbol{t}_{s,N} \right\rangle_{\Gamma_{s,N}^0}. \tag{3.18}$$

3.2.2. Variational form for the fluid problem

For the fluid flow problem, the velocity and pressure spaces are defined as $\mathbb{V} \subset H^1\left(\Omega_f\right)^d$ satisfying the Dirichlet conditions and $\mathbb{Q} = L^2\left(\Omega_f\right)$, respectively. Let also $\mathbb{V}_0 \subset H^1\left(\Omega_f\right)^d$ be the space of functions that vanish on the Dirichlet boundary of the fluid domain $\Gamma_{f,D}^0$. Let $\mathbb{X} := \mathbb{V} \times \mathbb{Q}$ and $\mathbb{X}_0 := \mathbb{V}_0 \times \mathbb{Q}$, so that the unknowns $\boldsymbol{U}_f = \left[\boldsymbol{u}_f, p_f\right]^T \in \mathbb{X}$ for each time t and the test functions $\boldsymbol{V}_f = \left[\boldsymbol{v}_f, q_f\right]^T \in \mathbb{X}_0$. By testing Eqs. (3.11)-(3.12) against arbitrary test functions $\boldsymbol{V}_f$, the weak form of the problem consists of finding $\boldsymbol{U}_f : \,]0, t_f[\,\to \mathbb{X}$ such that the initial conditions are satisfied and

$$\left\langle \boldsymbol{v}_f, \rho_f \frac{\partial \boldsymbol{u}_f}{\partial t} \right\rangle + \mathcal{A}_f\left(\boldsymbol{V}_f, \boldsymbol{U}_f\right) = \mathcal{F}_f\left(\boldsymbol{V}_f\right) \quad \forall \boldsymbol{V}_f \in \mathbb{X}_0, \tag{3.19}$$

where $\mathcal{A}_f\left(\boldsymbol{V}_f, \boldsymbol{U}_f\right)$ is a semilinear form defined on $\mathbb{X} \times \mathbb{X}_0$ as

$$\mathcal{A}_f\left(\boldsymbol{V}_f, \boldsymbol{U}_f\right) = \left\langle \boldsymbol{v}_f, \rho_f \boldsymbol{u}_f \cdot \nabla \boldsymbol{u}_f \right\rangle + \left\langle \nabla^s \boldsymbol{v}_f, 2\mu_f \nabla^s \boldsymbol{u}_f \right\rangle - \left\langle \nabla \cdot \boldsymbol{v}_f, p_f \right\rangle + \left\langle q, \nabla \cdot \boldsymbol{u} \right\rangle \tag{3.20}$$

and $\mathcal{F}_f\left(\boldsymbol{V}_f\right)$ is a linear form on $\mathbb{X}_0$ defined by

$$\mathcal{F}_f\left(\boldsymbol{V}_f\right) = \left\langle \boldsymbol{v}_f, \boldsymbol{f}_f \right\rangle + \left\langle \boldsymbol{v}_f, \boldsymbol{t}_{f,N} \right\rangle_{\Gamma_{f,N}}. \tag{3.21}$$

4. Time integration and linearization

In order to create a proper linear system of equations once discretized in space, the variational forms defined in Eqs. (3.16) and (3.19) need further treatment. In both cases the time derivative term has to be properly approximated using a time integration scheme. In the solid case, the geometric and material stiffness terms have to be linearized (first and third terms of Eq. (3.17)), while in the fluid case, only the convective term has to be linearized (first term in Eq. (3.20)). The time integration and linearization of each individual problem is described below.

4.1. Time integration

The time integration is performed by using an implicit scheme of the Backward Differentiation Formula (BDF) type for both solid and fluid problems. As usual, first order time integration (BDF1) is used to initialize computations, and it is followed by a second order time integration (BDF2) for the rest of the problem.

For this purpose, consider n as the time step counter and δt is the time step size of the uniform partition of the time interval $]0, T[$, and $\mathcal{O}(\cdot)$ is the approximation order of the scheme depending on the time step size. For the solid part, the second time derivative of the displacement $\frac{\partial^2 \boldsymbol{u}_s}{\partial t^2} =: \boldsymbol{a}_s$ is approximated at a given time step $t^{n+1} = t^n + \delta t$ as

$$\text{BDF1}: \qquad \boldsymbol{a}_s^{n+1} = \frac{1}{\delta t^2}\left[\boldsymbol{u}_s^{n+1} - 2\boldsymbol{u}_s^n + \boldsymbol{u}_s^{n-1}\right] + \mathcal{O}(\delta t), \tag{4.1}$$

$$\text{BDF2}: \qquad \boldsymbol{a}_s^{n+1} = \frac{1}{\delta t^2}\left[2\boldsymbol{u}_s^{n+1} - 5\boldsymbol{u}_s^n + 4\boldsymbol{u}_s^{n-1} - \boldsymbol{u}_s^{n-2}\right] + \mathcal{O}(\delta t^2). \tag{4.2}$$

Similarly for the fluid part, the first time derivative of the velocity $\frac{\partial \boldsymbol{u}_f}{\partial t} =: \boldsymbol{a}_f$ is computed as

$$\text{BDF1}: \qquad \boldsymbol{a}_f^{n+1} = \frac{1}{\delta t}\left[\boldsymbol{u}_f^{n+1} - \boldsymbol{u}_f^n\right] + \mathcal{O}(\delta t), \tag{4.3}$$

$$\text{BDF2}: \qquad \boldsymbol{a}_f^{n+1} = \frac{1}{2\delta t}\left[3\boldsymbol{u}_f^{n+1} - 4\boldsymbol{u}_f^n + \boldsymbol{u}_f^{n-1}\right] + \mathcal{O}\left(\delta t^2\right). \tag{4.4}$$

4.2. Linearization

The finite strain solid mechanics equations yield a non-linear system that must be linearized in order to be solved. The idea is to obtain a bilinear operator that allows to compute a correction $\delta \boldsymbol{U}_s := \left[\delta \boldsymbol{u}_s, \delta \boldsymbol{S}_s\right]^T$ of the guessed solution $\boldsymbol{U}_s^{n+1}$ at a time t^{n+1}. The linearization is performed by using a Newton-Raphson scheme on the formulation presented in Eq. (3.16), meaning that the unknown for which we solve becomes the correction of the solution. Therefore the new problem consists in finding $\delta \boldsymbol{U}_s \in \mathbb{W}_0$ such that

$$\left\langle \boldsymbol{v}_s, \rho_s^0 \frac{c_s}{\delta t^2} \delta \boldsymbol{u}_s \right\rangle + \mathcal{B}_s\left(\boldsymbol{V}_s, \delta \boldsymbol{U}_s\right) = \mathcal{F}_s\left(\boldsymbol{V}_s\right) - \mathcal{A}_s\left(\boldsymbol{V}_s, \boldsymbol{U}_s^{n+1}\right) - \left\langle \boldsymbol{v}_s, \rho_s^0 \boldsymbol{a}_s^{n+1} \right\rangle \quad \forall \boldsymbol{V}_s \in \mathbb{W}_0, \tag{4.5}$$

where $\mathcal{B}_s\left(\boldsymbol{V}_s, \delta \boldsymbol{U}_s\right)$ defined on $\mathbb{W}_0 \times \mathbb{W}_0$ is the bilinear form obtained through the linearization of $\mathcal{A}_s\left(\boldsymbol{V}_s, \boldsymbol{U}_s\right)$, and it is defined as

$$\mathcal{B}_s\left(\boldsymbol{V}_s,\delta\boldsymbol{U}_s\right)=\left\langle\frac{\partial v_{s_a}}{\partial X_A},\frac{\partial\delta u_{s_a}}{\partial X_B}S_{s_{BA}}\right\rangle+\left\langle\frac{\partial v_{s_a}}{\partial X_A},F_{s_{aB}}\delta S_{s_{BA}}\right\rangle+\left\langle T_{s_{AB}},\delta S_{s_{AB}}\right\rangle-\left\langle T_{s_{AB}},\mathbb{C}_{s_{ABCD}}F_{s_{aC}}\frac{\partial\delta u_{s_a}}{\partial X_D}\right\rangle, \tag{4.6}$$

where $\mathbb{C}_s=4\frac{\partial^2\Psi_s}{\partial\boldsymbol{C}_s\partial\boldsymbol{C}_s}$ is the constitutive tangent matrix which relates variations of the PK2 stress tensor $\delta\boldsymbol{S}_s$ and the right Cauchy tensor $\delta\boldsymbol{C}_s$. In the same manner, the time derivative term is linearized as

$$\left.\frac{\partial^2\boldsymbol{u}}{\partial t^2}\right|_{t^{n+1}}=\frac{c_s}{\delta t^2}\delta\boldsymbol{u}+\boldsymbol{a}^{n+1}, \tag{4.7}$$

where c_s is a coefficient that depends on the integration scheme ($c_s=1$ for BDF1 and $c_s=2$ for BDF2), and $\boldsymbol{a}_s^{n+1}$ is the acceleration obtained in the previous iteration, computed as stated in Eqs. (4.1) and (4.2). The bilinear form $\mathcal{B}_s$ relies on the previous iteration values of the unknown $\boldsymbol{U}_s^{n+1}$ through the evaluation of various tensor functions, although this dependence has not been explicitly presented.

The Navier-Stokes equations have a non-linearity in the convective term presented in Eq. (3.16), that can be linearized using a proper scheme. In this work, both fixed point and Newton-Raphson schemes are considered. Let us consider $\hat{\boldsymbol{u}}_f$ to be the previous iteration velocity in a given time step and c_l a constant that determines the type of linearization. The linearized problem consists in finding $\boldsymbol{U}_f\in\mathbb{X}$ such that

$$\left\langle\boldsymbol{v}_f,\rho_f\boldsymbol{a}_f\right\rangle+\mathcal{B}_f\left(\boldsymbol{V}_f,\boldsymbol{U}_f\right)=\mathcal{F}_f\left(\boldsymbol{V}_f\right)-c_l\left\langle\boldsymbol{v}_f,\rho_f\hat{\boldsymbol{u}}_f\cdot\nabla\hat{\boldsymbol{u}}_f\right\rangle\quad\forall\boldsymbol{V}_f\in\mathbb{X}_0, \tag{4.8}$$

where $\mathcal{B}_f$ is a bilinear form defined as

$$\mathcal{B}_f\left(\boldsymbol{V}_f,\boldsymbol{U}_f\right)=\left\langle\boldsymbol{v}_f,\rho_f\hat{\boldsymbol{u}}_f\cdot\nabla\boldsymbol{u}_f\right\rangle+c_l\left\langle\boldsymbol{v}_f,\rho_f\boldsymbol{u}_f\cdot\nabla\hat{\boldsymbol{u}}_f\right\rangle+\left\langle\nabla^s\boldsymbol{v}_f,2\mu_f\nabla^s\boldsymbol{u}_f\right\rangle-\left\langle\nabla\cdot\boldsymbol{v}_f,p_f\right\rangle+\left\langle q,\nabla\cdot\boldsymbol{u}\right\rangle, \tag{4.9}$$

and the values $c_l=0$ and $c_l=1$ set the linearization as fixed point and Newton-Raphson schemes, respectively.

5. Stabilized finite element formulation

Given that the primary objective of this work is not to introduce the already established stabilized formulation that we use, the details regarding the mathematical foundations are omitted. The stabilized formulation adopted here follows the Variational Multiscale (VMS) framework, initially proposed by Hughes et al. [45] and further developed in [46]. The fundamental concept within this framework is incorporating additional consistent terms into the original Galerkin FE formulation, enhancing its stability without compromising accuracy. This enhancement is achieved by introducing a finer resolution space, known as the sub-grid scale (SGS) space.

Let us start with the standard Galerkin FE approximation of the variational problem defined in Eqs. (4.5) for the solid and in Eq. (4.8) for the fluid. In a general manner, if we consider a FE partition $\mathcal{P}_h$ of a domain Ω, the diameter of an element domain $K\in\mathcal{P}_h$ is denoted by h_K, and the diameter of the element partition is defined as $h=\max\left\{h_K|K\in\mathcal{P}_h\right\}$. Under this definition, the FE partitions of the solid and fluid domains will be denoted as $\mathcal{P}_h^s$ and $\mathcal{P}_h^f$, respectively.

5.1. Finite strain stabilized formulation

The conforming FE spaces of the solid domain are constructed in the usual manner $\mathbb{U}_h\subset\mathbb{U}$ and $\mathbb{T}_h\subset\mathbb{T}$; therefore $\mathbb{W}_h=\mathbb{U}_h\times\mathbb{T}_h$. The subspace of $\mathbb{U}_h$ of vectors that vanish on the Dirichlet boundary is denoted as $\mathbb{U}_{h,0}\subset\mathbb{U}_0$, and $\mathbb{W}_{h,0}=\mathbb{U}_{h,0}\times\mathbb{T}_h$. Therefore, the Galerkin FE approximation consists of finding $\delta\boldsymbol{U}_{s,h}=\left[\delta\boldsymbol{u}_{s,h},\delta\boldsymbol{S}_{s,h}\right]^T\in\mathbb{W}_{h,0}$ for a time t^{n+1}, such that

$$\left\langle\boldsymbol{v}_{s,h},\rho_s^0\frac{c_s}{\delta t^2}\delta\boldsymbol{u}_{s,h}\right\rangle+\mathcal{B}_s\left(\boldsymbol{V}_{s,h},\delta\boldsymbol{U}_{s,h}\right)=\mathcal{F}_s\left(\boldsymbol{V}_{s,h}\right)-\mathcal{A}_s\left(\boldsymbol{V}_{s,h},\boldsymbol{U}_{s,h}^{n+1}\right)-\left\langle\boldsymbol{v}_{s,h},\rho_s^0\boldsymbol{a}_s^{n+1}\right\rangle\quad\forall\boldsymbol{U}_{s,h}\in\mathbb{W}_{h,0}. \tag{5.1}$$

The Galerkin FE approximation lacks of stability unless particular interpolations are used to interpolate the displacement and PK2 stress fields, requiring to satisfy appropriate inf-sup conditions which can be achieved by means of stabilization [42]. The stabilized formulation using the VMS approach for the solid mechanics problem has been initially developed for the finite strain solids for the three-field formulations to obtain enhanced precision in the stress field and to circumvent the numerical locking due to incompressibility [44]. It has also been extended to solid-shell elements in order to formulate a locking-free approach in the approximation of thin structures [41].

For the mixed finite strain solid formulation we choose the SGS space to be the orthogonal complement to the FE space, namely, we use the Orthogonal Subgrid Scale formulation (OSGS), which yields

$$\left\langle\boldsymbol{v}_{s,h},\rho_s^0\frac{c_s}{\delta t^2}\delta\boldsymbol{u}_{s,h}\right\rangle+\mathcal{B}_s\left(\boldsymbol{V}_{s,h},\delta\boldsymbol{U}_{s,h}\right)+\sum_K\left\langle\mathrm{L}^s\left(\boldsymbol{V}_{s,h}\right),\tau_K\mathrm{R}_{\delta\boldsymbol{U}}^s\left(\delta\boldsymbol{U}_{s,h}\right)\right\rangle_K$$
$$=\mathcal{F}_s\left(\boldsymbol{V}_{s,h}\right)-\mathcal{A}_s\left(\boldsymbol{V}_{s,h},\boldsymbol{U}_{s,h}^{n+1}\right)-\left\langle\boldsymbol{v}_{s,h},\rho_s^0\boldsymbol{a}_s^{n+1}\right\rangle$$
$$-\sum_K\left\langle\mathrm{L}^s\left(\boldsymbol{V}_{s,h}\right),\tau_K\left[\mathrm{R}_{\boldsymbol{U}}^s\left(\boldsymbol{U}_{s,h}^{n+1}\right)-\Pi^h\left(\mathrm{R}_{\boldsymbol{U}}^s\left(\boldsymbol{U}_{s,h}^{n+1}\right)\right)\right]\right\rangle_K, \tag{5.2}$$

where Π^h is the L^2 projection onto the FE space and $L^s = \left[L_u^s, L_S^s \right]^T$ is the adjoint operator that comes from the integration by parts of $\mathcal{B}_s$, defined by components as

$$L_u^s \left(\boldsymbol{V}_{s,h} \right)_a = -\frac{\partial}{\partial X_B} \left\{ \frac{\partial v_{s,h_a}}{\partial X_A} S_{s,h_{BA}} \right\} + \frac{\partial}{\partial X_D} \left\{ T_{s_{AB}} \mathbb{C}_{s_{ABCD}} F_{s_{aC}} \right\},$$

$$L_S^s \left(\boldsymbol{V}_{s,h} \right)_{AB} = \frac{\partial v_{s,h_a}}{\partial X_A} F_{s_{aB}} + T_{s_{AB}}.$$

The residual operators $R_{\delta U}^s$ and R_U^s are defined as

$$R_{\delta U}^s \left(\delta \boldsymbol{U}_{s,h} \right) = -B^s \left(\delta \boldsymbol{U}_{s,h} \right),$$

$$R_U^s \left(\boldsymbol{U}_{s,h}^{n+1} \right) = F^s - A^s \left(\boldsymbol{U}_{s,h}^{n+1} \right),$$

where the components of $B^s = \left[B_u^s, B_S^s \right]^T$, $A^s = \left[A_u^s, A_S^s \right]^T$, and $F^s = \left[F_u^s, F_S^s \right]^T$ are defined as

$$B_u^s \left(\delta \boldsymbol{U}_{s,h} \right)_a = -\frac{\partial}{\partial X_A} \left\{ \frac{\delta u_{s,h_a}}{\partial X_B} S_{s,h_{AB}} \right\} - \frac{\partial}{\partial X_A} \left\{ F_{s_{aB}} \delta S_{s,h_{AB}} \right\},$$

$$B_S^s \left(\delta \boldsymbol{U}_h \right)_{AB} = \delta S_{s,h_{AB}} - \mathbb{C}_{s_{ABCD}} F_{s_{aC}} \frac{\partial \delta u_{s,h_a}}{\partial X_D},$$

$$A_u^s \left(\boldsymbol{U}_h^{n+1} \right)_a = -\frac{\partial}{\partial X_A} \left\{ F_{s_{aB}} S_{s,h_{BA}} \right\},$$

$$A_S^s \left(\boldsymbol{U}_{s,h}^{n+1} \right)_{AB} = S_{s,h_{AB}} - 2 \frac{\partial \Psi}{\partial C_{s,AB}},$$

$$F_{u_a}^s = \rho_s^0 b_{s_a},$$

$$F_S^s = 0.$$

It is understood that $\boldsymbol{F}_s$ and $\boldsymbol{C}_s$ are computed with $\boldsymbol{u}_{s,h}$. Tensor $\mathbb{C}_s$ is the fourth order tangent constitutive tensor.

The matrix $\boldsymbol{\tau}_K^{-1}$ is an approximation of the operator B^s withing each element K. The details on how to design $\boldsymbol{\tau}_K$ can be reviewed in [47]. In this case, $\boldsymbol{\tau}_K$ is taken as a diagonal matrix where the stabilization parameters are

$$\boldsymbol{\tau}_K = \begin{bmatrix} \tau_u \boldsymbol{I}_d & \boldsymbol{0} \\ \boldsymbol{0} & \tau_S \boldsymbol{I} \end{bmatrix}, \qquad \tau_u = c_u \frac{h_K^2}{2\mu_s}, \qquad \tau_S = c_S,$$

where c_u and c_S are algorithmic parameters to be chosen. In the examples below they are set as $c_u = 0$ and $c_S = 0.1$, although it has been proven that the formulation is very insensitive to them, and they can be set in a wide range of values. It has to be noted that this expression of the stabilization parameters mimics the classical primal formulation of the mixed problem in the linear (infinitesimal strain) case [48]. The possibility of using other expressions with better convergence behavior in finite strain problems needs to be explored.

5.2. Navier-Stokes stabilized formulation

The standard Galerkin approximation of the Navier-Stokes can be constructed using conforming FE spaces for the velocity $\mathbb{V}_h \subset \mathbb{V}$, the velocity test functions $\mathbb{V}_{h,0} \subset \mathbb{V}_0$ and the pressure $\mathbb{Q}_h \subset \mathbb{Q}$, in the usual manner. If $\mathbb{X}_h := \mathbb{V}_h \times \mathbb{Q}_h$ and $\mathbb{X}_{h,0} := \mathbb{V}_{h,0} \times \mathbb{Q}_h$, the Galerkin FE approximation consists of finding $\boldsymbol{U}_{f,h} = \left[\boldsymbol{u}_{f,h}, p_{f,h} \right]^T$ for a time t^{n+1} such that

$$\left\langle \boldsymbol{v}_{f,h}, \rho_f \boldsymbol{a}_{f,h} \right\rangle + \mathcal{B}_f \left(\boldsymbol{V}_{f,h}, \boldsymbol{U}_{f,h} \right) = \mathcal{F}_f \left(\boldsymbol{V}_{f,h} \right) - c_l \left\langle \boldsymbol{v}_{f,h}, \rho_f \hat{\boldsymbol{u}}_{f,h} \cdot \nabla \hat{\boldsymbol{u}}_{f,h} \right\rangle \quad \forall \boldsymbol{V}_{f,h} \in \mathbb{X}_{h,0}. \tag{5.3}$$

It is well known that the approximation in Eq. (5.3) has numerical instabilities that need to be addressed. The first one arises when the nonlinear convective term dominates the viscous term, giving place to spurious boundary layers. The second one is the incompatibility of $\mathbb{V}_h \times \mathbb{Q}_h$ which arises when using equal order interpolation, and therefore the discrete compatibility or inf-sup condition is not satisfied. However, these can be overcome by using the VMS approach presented below. This kind of stabilized formulations have been long established for the Navier-Stokes problem, including compressible [49] and incompressible flows [50], as well as viscoelastic fluids [51,52]. A complete review on this approach can be found in [53].

For the stabilized Navier-Stokes formulation we choose the projection of the SGS to be the identity on the space of FE residuals, resulting in the Algebraic Subgrid Scale formulation (ASGS), which yields

$$\left\langle \boldsymbol{v}_{f,h}, \rho_f \boldsymbol{a}_{f,h} \right\rangle + \mathcal{B}_f \left(\boldsymbol{V}_{f,h}, \boldsymbol{U}_{f,h} \right) - \sum_K \left\langle L^f \left(\boldsymbol{V}_{f,h} \right), \boldsymbol{\alpha}_K R^f \left(\boldsymbol{U}_{f,h} \right) \right\rangle_K$$

$$= \mathcal{F}_f \left(\boldsymbol{V}_{f,h} \right) - c_l \left\langle \boldsymbol{v}_{f,h}, \rho_f \hat{\boldsymbol{u}}_{f,h} \cdot \nabla \hat{\boldsymbol{u}}_{f,h} \right\rangle \quad \forall \boldsymbol{V}_{f,h} \in \mathbb{X}_{h,0}, \tag{5.4}$$

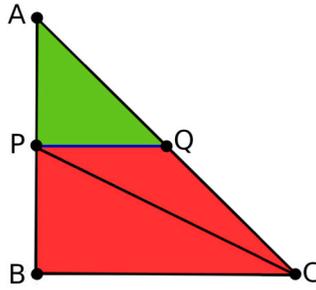where $L^f = \left[L_u^f, L_p^f \right]^T$ is the adjoint operator that comes from the integration by parts of $\mathcal{B}_f$ defined as

Fig. 3. Partition of a triangle element into sub-elements following the interface.

$$L_u^f \left(\boldsymbol{V}_{f,h} \right) = -\rho_f \hat{\boldsymbol{u}}_{f,h} \cdot \nabla \boldsymbol{v}_{f,h} - \nabla \cdot \left(2\mu_f \nabla^s \boldsymbol{v}_{f,h} \right) - \nabla q_{f,h},$$

$$L_p^f \left(\boldsymbol{V}_{f,h} \right) = \nabla \cdot \boldsymbol{v}_{f,h},$$

and the residual R^f is defined as

$$R^f \left(\boldsymbol{U}_{f,h} \right) = F^f - B^f \left(\boldsymbol{U}_{f,h} \right),$$

where the components of $B^f = \left[B_u^f, B_p^f \right]^T$ and $F^f = \left[F_u^f, F_p^f \right]^T$ are defined as

$$B_u^f \left(\boldsymbol{U}_{f,h} \right) = \rho_f \hat{\boldsymbol{u}}_f \cdot \nabla \boldsymbol{u}_{f,h} - \nabla \cdot \left(2\mu_f \nabla^s \boldsymbol{u}_{f,h} \right) + \nabla p_{f,h},$$

$$B_p^f \left(\boldsymbol{U}_{f,h} \right) = -\nabla \cdot \boldsymbol{u}_{f,h},$$

$$F_u^f = \boldsymbol{f}_f,$$

$$F_p^f = 0,$$

and the matrix $\boldsymbol{\alpha}_K$ of stabilization parameters is computed as

$$\boldsymbol{\alpha}_K = \begin{bmatrix} \alpha_u \boldsymbol{I}_d & \boldsymbol{0} \\ \boldsymbol{0} & \alpha_p \end{bmatrix}, \qquad \alpha_u = \left[c_1 \frac{\mu_f}{h_K^2} + c_2 \frac{\rho_f \left| \hat{\boldsymbol{u}}_f \right|}{h_K} \right]^{-1}, \qquad \alpha_p = \frac{h_K^2}{\alpha_u},$$

where $\left| \hat{\boldsymbol{u}}_f \right|$ is the Euclidean norm of the velocity guess, and the algorithmic parameters are chosen as $c_1 = 4$ and $c_2 = 2$ for linear elements.

6. Discontinuous shape functions

The pressure discontinuities in the fluid domain arising due to the presence of a solid interface embedded in it are addressed by using the discontinuous shape functions presented by Ausas et al. in [54]. These shape functions facilitate the segregation of degrees of freedom within an element into two entirely independent parts, with no additional treatment required for neighboring elements. This local implementation simplifies the construction of discontinuous shape functions, applying the same principles to both triangles and tetrahedral elements. This approach is convenient at the computational level, because it does not require to add additional degrees of freedom, which avoids the need of recomputing the domain's graph at each time step. For simplicity, only a brief summary of the implementation for triangular elements is provided.

Consider a triangle ABC, whose edges $\bar{AB}$ and $\bar{AC}$ are cut by the interface at points P and Q respectively. We wish to construct a FE basis that is discontinuous across PQ. As illustrated in Fig. 3, the element is divided into a positive (green) and a negative (red) side. At the same time, the element is divided into sub-elements that follow the interface: in this case the sub-triangles are arbitrarily created as APQ, CQP and BCP. To achieve a discontinuous approximation, the shape functions on the green side must exclusively depend on the nodes belonging to the green side, while the shape functions on the red side must solely depend on the nodes that belong to the red side. This explanation may seem redundant, but it is crucial to the construction of discontinuous functions. Let N^A, N^B and N^C be the shape functions of nodes A, B and C of a triangular element. The basic idea is to "carry" the values of N^A, N^B and N^C through their adjacent edges in their respective sides. By this logic, the discontinuous shape functions take the form illustrated in Fig. 4, constructed as follows: point A is the only point available at the green side; therefore, the value of the shape function N^A at point A is carried to points P and Q, and it is zero along the red side. The red side has points B and C; therefore, N^B carries its value from B to P and N^C carries its value from C to Q, and are zero along the green side.

Let P^+ and P^- be the coordinates of point P reached from the green and the red sides of the triangle, respectively, and likewise for Q^+ and Q^-. With the above modifications, the discontinuous shape functions take the following values at the nodes:

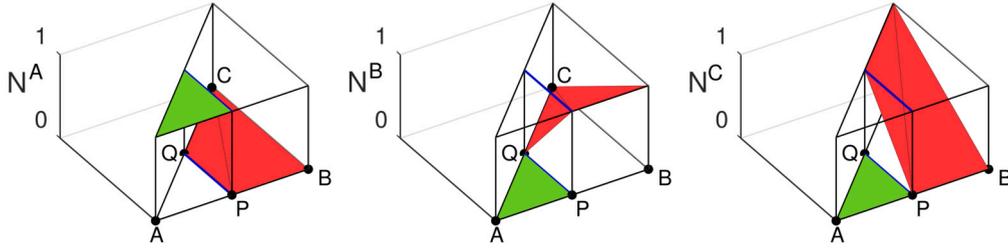$$N^A(A) = 1, \qquad N^B(A) = 0, \qquad N^C(A) = 0,$$

Fig. 4. Discontinuous shape functions for cut elements.

$$N^A(B) = 0, \qquad N^B(B) = 1, \qquad N^C(B) = 0,$$

$$N^A(C) = 0, \qquad N^B(C) = 0, \qquad N^C(C) = 1,$$

$$N^A(P^+) = 1, \qquad N^B(P^+) = 0, \qquad N^C(P^+) = 0,$$

$$N^A(P^-) = 0, \qquad N^B(P^-) = 1, \qquad N^C(P^-) = 0,$$

$$N^A(Q^+) = 1, \qquad N^B(Q^+) = 0, \qquad N^C(Q^+) = 0,$$

$$N^A(Q^-) = 0, \qquad N^B(Q^-) = 0, \qquad N^C(Q^-) = 1.$$

It is important to remark that these discontinuous shape functions fulfill important properties:

- They form a nodal basis, their values are one at their respective nodes and zero at the other nodes.
- Their sum equals a constant function equal to one along the element.
- Their extreme values are one and zero, and take place at the nodes.

It is worth mentioning that derivatives are zero in certain parts of the element, as the shape functions remain constant on sides where the cut leaves only one node. This fact leads to an expected convergence rate of $\mathcal{O}\left(h^{3/2}\right)$ [54].

7. Fluid-structure interaction

7.1. Transmission conditions

The FSI problem addressed in this study employs a partitioned scheme, where the fluid and the solid are solved independently and coupled at the embedded interface. The solid domain is embedded within the fluid domain with non-matching interfaces. It is crucial to note that, from the fluid's perspective, the embedded interface is perceived as a surface in 3D and, by extension, as a line in 2D cases. In the construction of the solid domain, as detailed in Section 2, we use a volumeless surface of the solid domain Ω_s^{2D} as a reference to extrude a volumetric body for the solid-shell. For the transmission conditions, the same volumeless surface as the embedding interface is used. Therefore, the coupling interface is defined as $\Gamma_{\mathrm{cut}}(t) = \Omega_f(t) \bigcap \Omega_s^{2D}(t)$, where the Dirichlet-Neumann coupling conditions must be satisfied. The fluid is solved considering the position, displacement, and velocity of the solid-shell mid-surface, while the tractions acting on the solid are computed from the fluid. This is achieved through a block-iterative scheme, where the solid and the fluid are sequentially solved with strong coupling.

The coupling consists of kinematic and dynamic conditions to be fulfilled. Firstly, the kinematic transmission of no-slip wall condition is:

$$\boldsymbol{u}_f = \frac{\partial \boldsymbol{u}_s}{\partial t} \quad \text{on } \Gamma_{\mathrm{cut}}(t), \tag{7.1}$$

which ensures the continuity of the velocity in $\Omega_f(t)$ across $\Gamma_{\mathrm{cut}}(t)$. In other words, the fluid adjacent to the interface conducts the same movement as the solid. Secondly, the dynamic boundary condition of the equilibrium of surface tractions along the interface is:

$$\boldsymbol{n}_f \cdot \boldsymbol{\sigma}_f = \boldsymbol{n}_s \cdot \boldsymbol{\sigma}_s \qquad \text{on } \Gamma_{\mathrm{cut}}(t), \tag{7.2}$$

which is independently computed at both sides of the embedded interface, as illustrated in Fig. 5, where the symbols $+$ and $-$ represent the variables at the upper and lower surfaces, respectively.

A crucial aspect of our approach is that the coupling interface corresponds to the mid-surface of the solid-shell. By using this approximation, the process of transferring the shell velocity to the fluid is trivial because it only requires to pass the shell's mid-surface velocity. However, tractions require an special treatment due to the discontinuity of pressures and the limitations of the discontinuous shape functions. Firstly, as has already been explained in Section 6, due to the construction process of the discontinuous shape functions, its derivatives can be zero in one of the sides of the element. In fact, in the case of triangular elements there is always a zero-derivative in one of the sides. Consequently, computing the fluid tractions as $\boldsymbol{t}_f = \boldsymbol{n}_f \cdot \left(-p\boldsymbol{I} + 2\mu_f \nabla^s \boldsymbol{u}_f\right)$ is not consistent
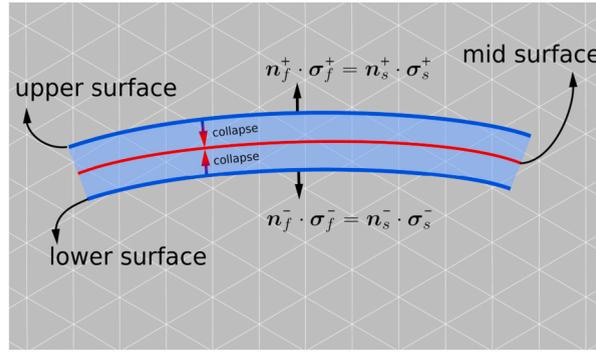
Fig. 5. Surface tractions computation.

because the velocity gradient cannot be captured at both sides of the embedded interface at the same time. For this reason, the approximation is performed by using only the pressure as

$$t_f = -\boldsymbol{n}_f p_f \qquad \text{on } \Gamma_{\text{cut}}(t). \tag{7.3}$$

Note that this limitation can be overcome by using enriched spaces for shape function derivatives in cut elements, as the one introduced in [55]. Likewise, velocity non-conformity can be dealt with using classical discontinuous Galerkin (DG) techniques (see below). Secondly, tractions have to be integrated independently at both sides of the embedded interface because they are physically independent of each other, and that is exactly what the discontinuous shape functions are trying to convey. Lastly, the traction integration is only performed at the mid-surface's normal direction and not in its transverse direction, as would occur at one of the ends of a cantilever bar. This approximation is justified because the effect of tractions in the transverse direction of the shell should be small for thin structures. However, as shown below in Section 8, the consequences of not including this contribution become apparent when the embedded structure is relatively thick.

7.2. Weak imposition of velocities

To enforce the velocity transmission condition described in Eq. (7.1) on the fluid, several options are available. One option involves creating new nodes in the element cuts, requiting a local re-meshing of the fluid mesh. However, this approach requires the activation and deactivation of new nodes whenever the mesh cutting process is performed. The mesh cutting process is performed on every coupling iteration, which is very expensive from the computational standpoint. In this work, the chosen option involves the use of discontinuous shape functions configured at element level, which allows the use of the same degrees of freedom already present in the fluid element. Considering that the discontinuous shape functions already take into account the embedded interface, the prescription of weak Dirichlet boundary conditions can be easily imposed by means of Nitsche's method.

Let E_{cut}^h be the edges of $\mathcal{P}_h^f$ created by the intersections of Γ_{cut}, there is a contribution of boundary terms that appear when the differential equations are integrated by parts that vanish on regular boundaries. However, test functions $\boldsymbol{v}_{f,h}$ do not vanish in E_{cut} and must be considered. Nitsche's method consists in adding to the discrete variational form of the problem in Eq. (5.4) the following terms:

$$\sum_{E_{\text{cut}}} \left\langle \boldsymbol{v}_{f,h} , \, p_{f,h} \boldsymbol{n}_f - 2\mu_f \boldsymbol{n}_f \cdot \nabla^s \boldsymbol{u}_{f,h} \right\rangle + \sum_{E_{\text{cut}}} \left\langle -q_{f,h} \boldsymbol{n}_f - 2\mu_f \boldsymbol{n}_f \cdot \nabla^s \boldsymbol{v}_{f,h} , \, \boldsymbol{u}_{f,h} - \dot{\boldsymbol{u}}_{s,h} \right\rangle + \sum_{E_{\text{cut}}} \frac{\mu_N}{h_E} \left\langle \boldsymbol{v}_{f,h} , \, \boldsymbol{u}_{f,h} - \dot{\boldsymbol{u}}_s \right\rangle, \tag{7.4}$$

where $\dot{\boldsymbol{u}}_s$ is the velocity of the solid in the coupling interface. In Eq. (7.4), the first term comes precisely from the integration by parts, the second term is the adjoint consistency term, and the third term is the stabilization term. The adjoint consistency term is designed according to [56–58]. The stabilization term penalizes the restriction given by the boundary condition in Eq. (7.1) and is scaled by the characteristic length h_E of E_{cut} and the algorithmic parameter μ_N, which has units of viscosity, defined as

$$\mu_N = \mu_f + \rho_f h_E |\bar{\boldsymbol{u}}_f|, \tag{7.5}$$

where $\bar{\boldsymbol{u}}_f$ is the maximum velocity of the fluid domain computed in the previous iteration.

It is crucial to emphasize that integrating Nitsche's terms on both sides of the embedded interface is essential because the modified shape functions render them entirely independent of each other. Therefore, the interface where weak boundary conditions are imposed actually consists of two distinct decoupled overlapping interfaces.

In the present embedded approach, there are pressure discontinuities due to the embedded interface dividing the fluid domain, which are captured by using discontinuous shape functions in the elements cut by the interface. Furthermore, the velocity field is approximated by these functions in the cut elements, even if the velocity field is continuous. This approach opens up the possibility to impose other boundary conditions where the velocity field is not completely continuous, such as slip wall or wall law, where only the normal component of the velocity is continuous [59]. This approach is useful because having locally segregated velocities allows to avoid the instabilities associated to badly cut elements. However, the use of these functions in the velocity field, whose space is

a subspace $H^1 \left(\Omega_f \right)^d$, makes the formulation to be non-conforming. The way to deal with this non-conformity is the same as in DG techniques. The classical symmetric interior penalty method amounts to add a term similar to (7.4) but summing for all edges (faces, in 3D) of elements in which the discontinuous interpolation has been used, and replacing $\boldsymbol{u}_{f,h} - \dot{\boldsymbol{u}}_s$ by the jump in velocities and the flux operators by the mean of the flux operators between adjacent elements [57]. However, being the non-conformity restricted to the band of elements crossed by the solid, we have numerically verified that it is not necessary to introduce the terms described.

7.3. Coupling strategy

Strongly coupled strategies require to ensure the convergence of the transmission conditions. This is typically achieved through Newton-Raphson iterative procedures known for their efficiency [60]. However, in this work, an Aitken relaxation scheme is implemented for simplicity, although it can be extended to more efficient methods [61]. Within each time step, this approach allows the application of dynamic relaxation to transmission conditions in each coupling iteration, thereby enhancing the convergence rate. The Aitken relaxation procedure computes an optimal relaxation parameter ω_{i+1} for each iteration $i+1$, such that coupling displacements are:

$$\boldsymbol{u}_{s,h}^{i+1} \leftarrow (1 - \omega_{i+1}) \boldsymbol{u}_{s,h}^{i+1} + \omega_{i+1} \boldsymbol{u}_{s,h}^{i}, \tag{7.6}$$

where ω_{i+1} is computed as follows:

1. At the beginning of a time step, set the initial relaxation parameter ω_0 and initialize Aitken's factor γ_i:
   $\omega_i = \omega_0.$
   $\gamma_i = 0.$
2. Compute the difference between the actual and previous iteration solutions:
   $\Delta \boldsymbol{u}_{s,h}^{i+1} = \boldsymbol{u}_{s,h}^{i+1} - \boldsymbol{u}_{s,h}^{i}.$
3. Compute Aitken's factor:
   $\gamma_{i+1} = \gamma_i + (\gamma_i - 1) \dfrac{\left(\Delta \boldsymbol{u}_{s,h}^{i} - \Delta \boldsymbol{u}_{s,h}^{i+1} \right)^T \Delta \boldsymbol{u}_{s,h}^{i+1}}{\left| \Delta \boldsymbol{u}_{s,h}^{i} - \Delta \boldsymbol{u}_{s,h}^{i+1} \right|^2}.$
4. Compute Aitken's optimal relaxation parameter:
   $\omega_{i+1} = 1 - \gamma_{i+1}.$
5. Update the iteration counter and all the arrays that depend on the iteration.

After the coupling strategy is performed, it is imperative to compute the coupling velocities based on the relaxed displacements. This approach enables the fluid to update the solution of a time step in a staggered manner, mitigating pressure spikes resulting from the movement of the embedding interface.

8. Numerical results

In this section, the embedded FSI approach is applied to classical benchmark problems commonly used in the literature. The summarized ingredients described throughout the work include: (i) the use of a locking-free formulation of solid-shell elements based on a mixed displacement-PK2 stress stabilization for finite strains, (ii) capturing the discontinuities of the fluid domain using discontinuous shape functions, (iii) weak imposition of boundary conditions at cut elements through Nitsche's method, and (iv) coupling the fluid and solid domains using Dirichlet-Neumann transmission conditions. However, to address them properly, they are tested in a staggered manner of increasing difficulty. Initially, the embedding technique and the weak imposition of boundary conditions are tested by solving fluid dynamic problems with a rigid stationary solid in a one-way coupling fashion. Using this approach, the coupling interface transmits zero velocity to the fluid, while tractions are not transmitted to the solid. First a stationary problem is solved and then a time-dependent one. Following this, a fully coupled FSI problem is solved with a deformable solid and complete transmission conditions. Using the same methodology, a dynamic problem that converges to a stationary solution is solved first, subsequently followed by a dynamic problem that exhibits a periodic solution.

8.1. Elbow pipe with internal wall

The initial example involves a 90°-curved elbow pipe with an internal zero-thickness rigid wall embedded inside the fluid domain, dividing the flow into two independent ducts. The internal wall is positioned such that the upper duct maintains a constant cross-section, while the lower duct contracts by half after the curvature. This contraction induces an acceleration of the flow, maintaining a constant total flow rate. This problem was initially proposed by Idelsohn et al. [62] using a slip interface as internal wall. However, as summarized in Fig. 6, here the no-slip interface version of the problem portrayed in [63] is solved, which is later extended to its 3D version.

The boundary conditions of the 2D case consist in no-slip conditions at the upper and lower walls, and the following velocities at the inlet:
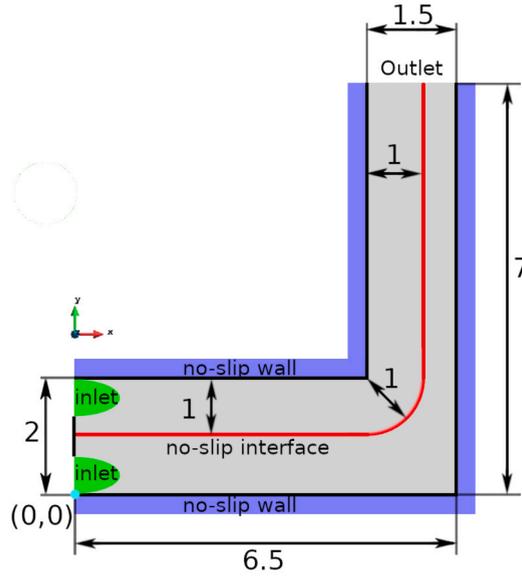
Fig. 6. 2D and 3D elbow with internal wall: geometry and boundary conditions.
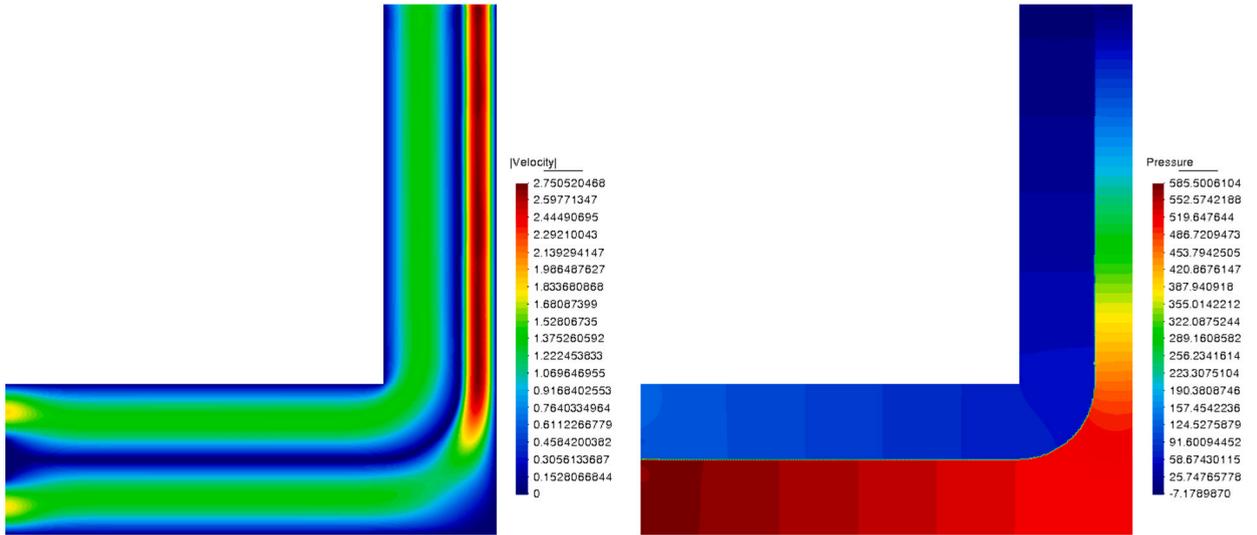

Fig. 7. 2D elbow with internal wall: (a) velocity and (b) pressure.

$$u_x(y) = \begin{cases} u_x^{\text{top}}(y) & \text{if } 1.25 < y < 2 \\ 0 & \text{if } 0.75 < y < 1.25 \\ u_x^{\text{bot}}(y) & \text{if } 0 < y < 0.75 \end{cases} \tag{8.1}$$

where u_x^{top} and u_x^{bot} are the parabolic velocities for the upper and lower inlets, defined as

$$u_x^{\text{top}}(y) = -12.642y^2 + 41.0864y - 31.6049, \tag{8.2}$$

$$u_x^{\text{bot}}(y) = -12.642y^2 + 9.4812y. \tag{8.3}$$

Note that only 75% of the width of the channel is set as inlet so it is not influenced by the discontinuous interpolation at the interface. For the 3D extension, slip lateral walls are used, so the solution is equivalent to the 2D counterpart. The problem is solved for Re = 1 using meshes of 122k unstructured triangular elements and 164k structured tetrahedral elements in the 2D and 3D cases, respectively. Note that the 3D mesh is much coarser than the 2D counterpart because of its additional dimension. Results are illustrated in Fig. 7 for the 2D case and in Fig. 8 for the 3D case.

The purpose of these examples is to illustrate how the pressure can be computed in a discontinuous manner through an interface. To show the discontinuity, in Fig. 9 the pressure along a transverse line located near the outlet is plotted, between coordinates
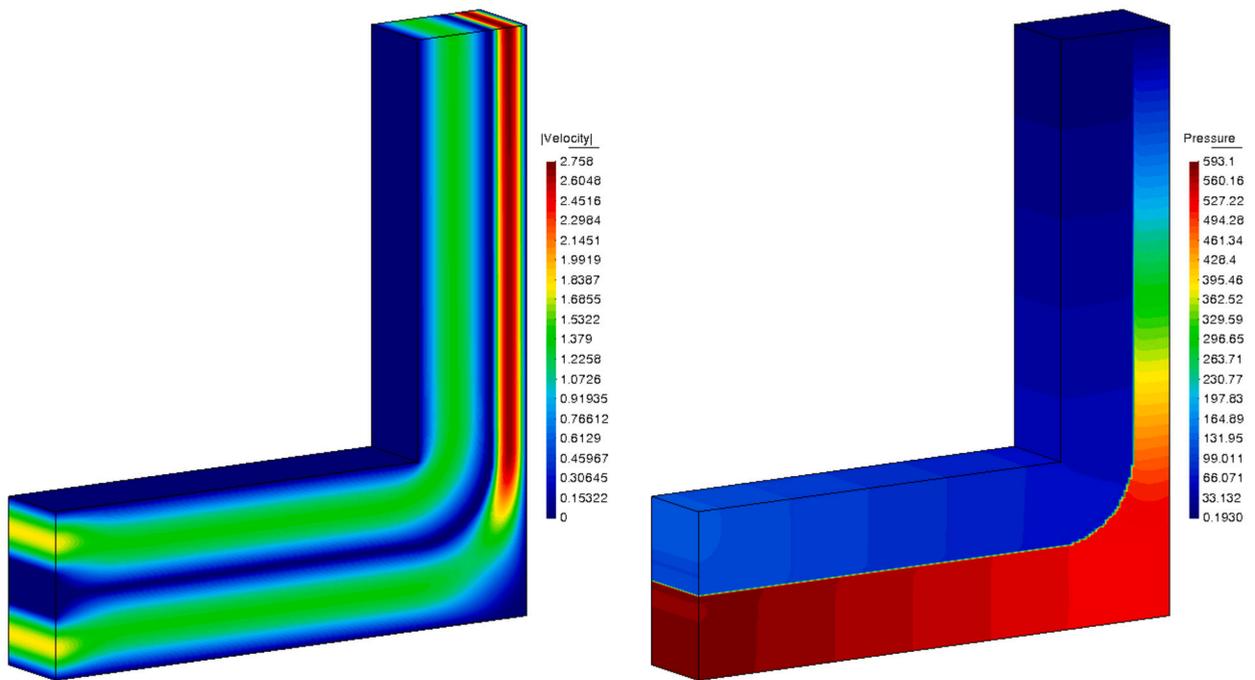
Fig. 8. 3D elbow with internal wall: (a) velocity and (b) pressure.
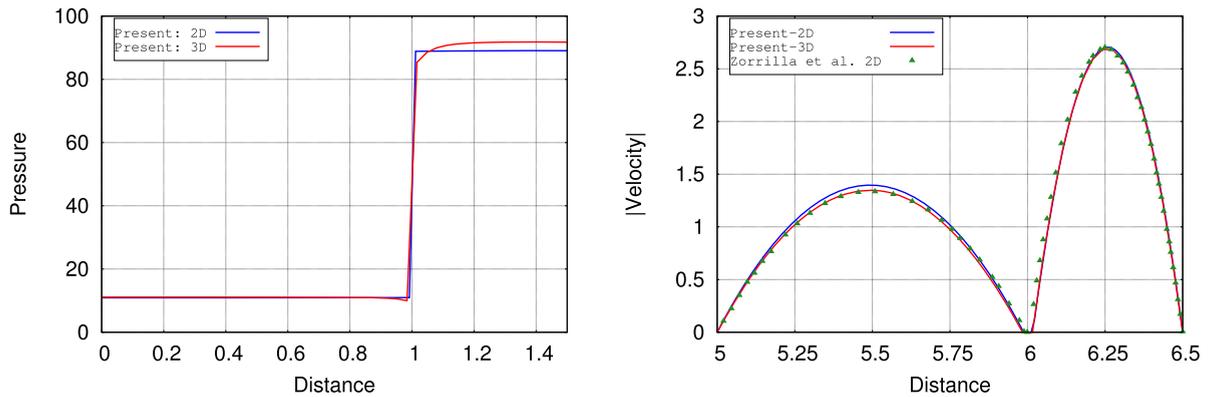
Fig. 9. Elbow pipe with internal wall: 2D and 3D elbow pressure through the coordinates $(5,6)$-$(6.5,6)$ and velocity magnitude at the outlet. References: Zorrilla et al. [63].

$(5,6)$-$(6.5,6)$, where the different pressures of each side of the duct can be clearly identified. The pressure jump in the 2D case is sharper when compared to the 3D case because of the better resolution provided by the mesh. In order to make more comprehensive comparisons, the velocity profiles are plotted at the outlet. Results show good agreement between the 2D and 3D versions and with respect to the reference solutions shown in [63].

An important aspect of the current embedded approach must be considered. Firstly, by weakly enforcing the velocity in the cut elements using Nitsche's method, the kinematic constraint is transferred to the nodes through the intersected edges. Secondly, the discontinuous shape functions of Ausas et al. have zero derivatives on one side of the cut, making this element unable to properly capture velocity gradients. Consequently, when enforcing a zero velocity constraint, as in this case, the condition is applied to the entire element, resulting in an artificial shrinkage of the duct [60]. A possible remedy is to use regular shape functions for the velocity space, though it comes with the hurdle of dealing with ill-conditioned elements when they are poorly cut. Nevertheless, the embedded approach is expected to converge to the solution obtained with a body-fitted approach with mesh refinement. Recall also the DG-like terms could be added, but we have found them unnecessary.
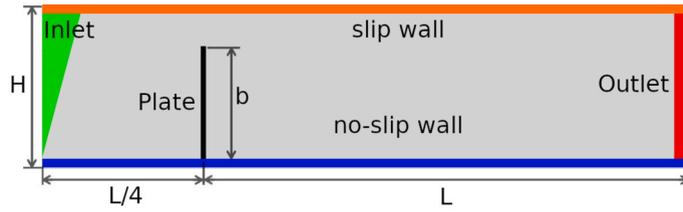
Fig. 10. 2D Vertical plate in a fluid tunnel - Geometry and boundary conditions.
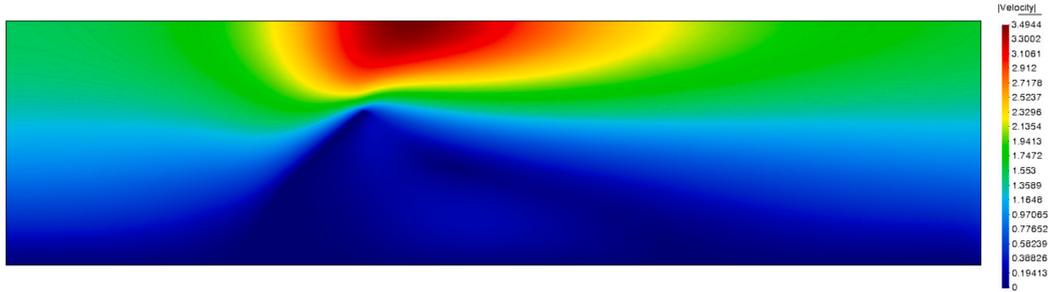
Fig. 11. 2D Vertical plate in a fluid tunnel - Stationary velocity magnitude.

8.2. Vertical plate in a fluid tunnel

The third example consists in a fluid flowing through a tunnel with a vertical hyperelastic plate partially blocking the flow. The solid is increasingly deformed by the fluid during the initial transient until it reaches a stationary solution. This case has been previously studied by Zhang et al. [64] and Hang et al. [65] in 2D and 3D environments, respectively. The geometry and boundary conditions are summarized in Fig. 10. For the present example, the reference values of $H = 1$, $L = 1$, $b = 0.8$ and the plate thickness $t_\text{p} = 0.04$ are used. The geometry is extended to 3D using a width of 0.5 for the tunnel and the plate.

The fluid domain boundary conditions consist in slip and no-slip walls for the top and bottom walls, respectively. The inlet velocity is set as a parabolic profile that increases along the *y*-axis using the following function:

$$u_f(0, y, 0, t) = \begin{cases} \hat{u}_f(0, y, 0) \dfrac{1 - \cos\left(\frac{\pi}{2} t\right)}{2} & \text{if } t < t_\text{init} \\ \hat{u}_f(0, y, 0) & \text{otherwise} \end{cases} ; \qquad \hat{u}_f(0, y, 0) = 1.5 \left(-y^2 + 2y\right),$$

considering the bottom left corner of the domain as the origin of the Cartesian coordinate system. Note that in order to have a smoother initial transient, a cosine time function is used to slowly increase the inlet velocity to reach its maximum using $t_\text{init} = 0.1$ for the 2D case and $t_\text{init} = 0.5$ for the 3D case. For the 3D extension of the problem, no-slip boundary conditions are used at the lateral walls of the tunnel. The problem is solved using a time step of $\delta t = 0.01$ in both cases. The domain of the 2D case is meshed with 35k linear triangular elements in the fluid and 300 line elements on the solid, which are extruded to 600 bilinear quadrilateral elements. Similarly, the domain of the 3D case is meshed with 235k linear tetrahedral elements in the fluid and 200 triangular elements on the solid, which are extruded to 1k linear prismatic elements. The solid boundary conditions consist in simply fixing the lower end of the plate, and fixing the plate displacements in the *z*-axis direction for the 3D case. The Dirichlet transmission conditions are set on the fluid by imposing the solid velocity on the elements cut by the interface, while the Neumann transmission conditions are set by imposing the fluid tractions on the whole plate. The properties of the fluid are $\rho_f = 1$ and $\mu_f = 0.1$, whereas the solid is configured as a compressible Neo-Hookean material with $\rho = 7.8$, $E = 10^5$ and $\nu = 0.3$.

The fluid velocity and pressure fields are displayed in Figs. 11-12 for the 2D case, and in Figs. 13-14 for the 3D case. For the solid domain, the vertical and horizontal displacement of the plate at its upper end is followed, as shown in Fig. 15 for the 2D and 3D cases. Considering that our shell formulation follows a mixed approach that uses displacements and the PK2 stress as unknowns, they are shown at the converged configuration in Figs. 16-17. Although there is no data to compare the displacements in the *y*-axis, there are some authors that have reported them in the *x*-axis [64,66,65]. Due to the different time functions used in the initial transient, there are slight differences in the time evolution results between the 3D and the 2D cases. There is a difference in the final stationary result, which can be attributed to the mesh refinement, which is much coarser than the one used in the 2D case.

8.3. Turek and Hron benchmark

The last example consists in one of the most widely used benchmark tests in the FSI context. It was designed by Turek and Hron in [67], with three different variants referred as FSI1, FSI2 and FSI3. In this example, the FSI2 variant is used as a reference. The case consists in a channel flow around an elastic bar attached to a rigid cylinder, which results in a self-induced oscillation. The domain
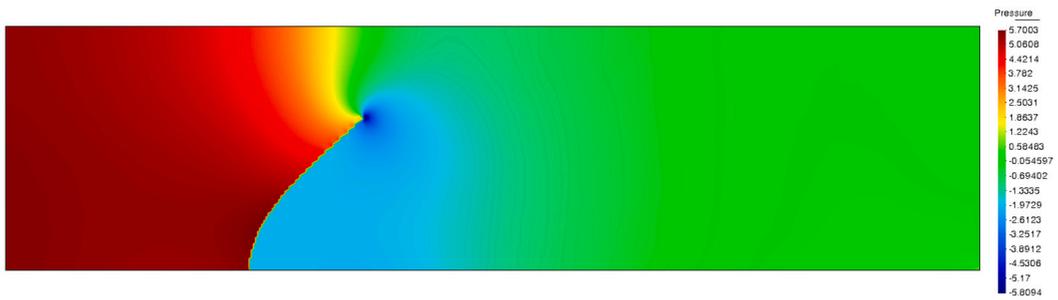
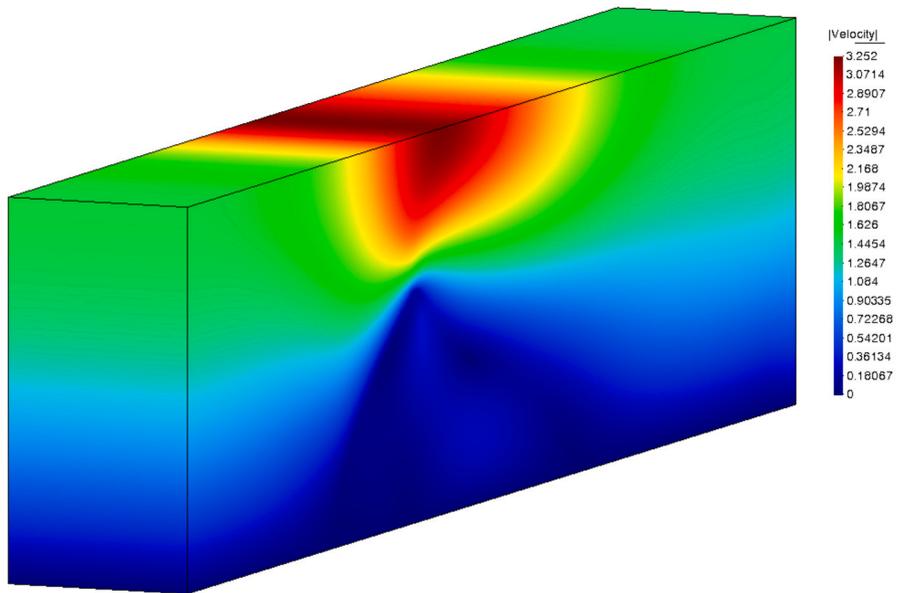**Fig. 12.** 2D Vertical plate in a fluid tunnel - Stationary pressure.

Fig. 13. 3D Vertical plate in a fluid tunnel - Stationary velocity magnitude.
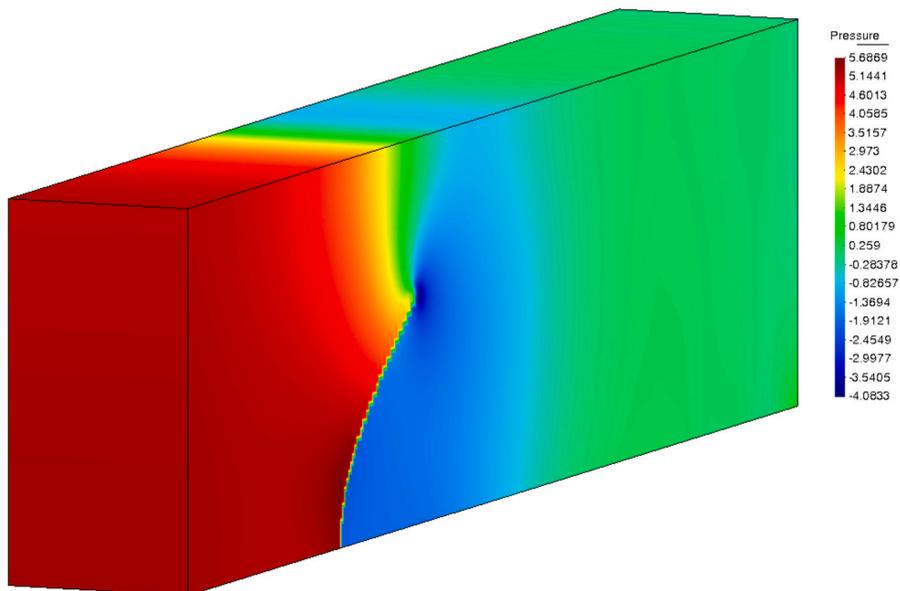

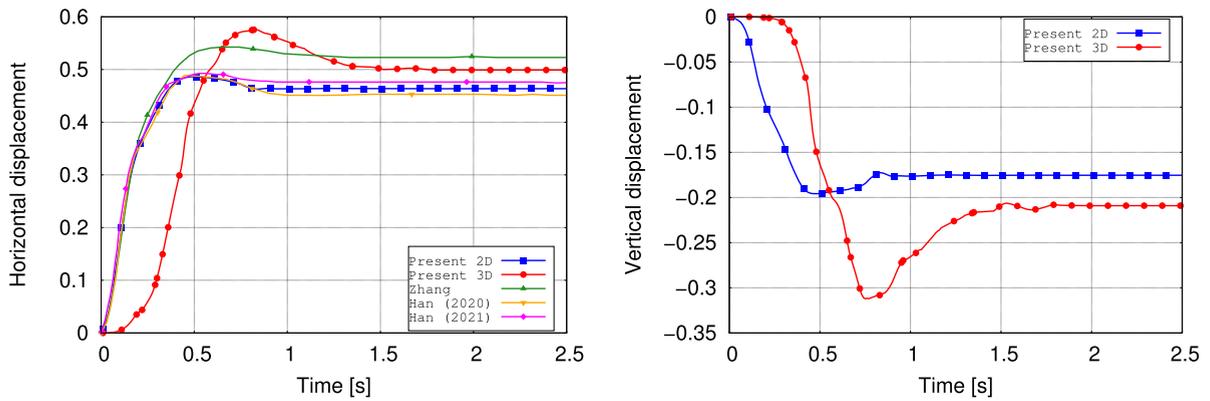**Fig. 14.** 3D Vertical plate in a fluid tunnel - Stationary pressure.

Fig. 15. Vertical plate in a fluid tunnel - Horizontal and vertical displacement at the upper end. References: Zhang et al. [64], Han et al. (2020) [66], Han et al. (2021) [65].
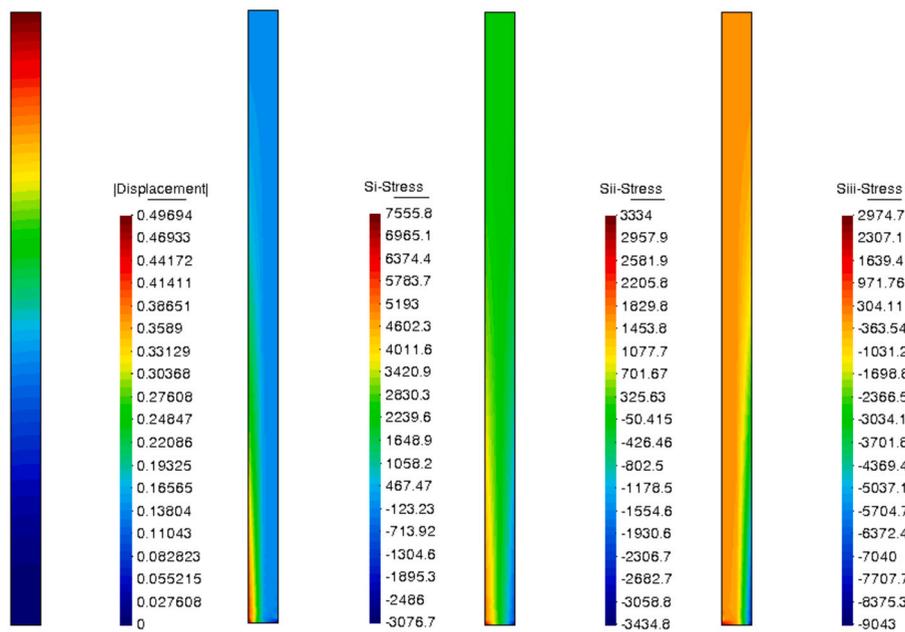

Fig. 16. 2D Vertical plate in a fluid tunnel - Displacement and principal PK2 stress fields.

and boundary conditions are summarized in Fig. 18. The domain dimensions for the fluid are set as $H = 0.41$, $L = 2.5$, $a = 0.2$, $b = 0.2$ and $D = 0.1$. The boundary conditions consist of no-slip conditions at the cylinder and the upper and lower walls, and the inlet velocity is prescribed with a parabolic profile given by

$$u_f(0, y, t) = \begin{cases} \hat{u}_f(0, y) \dfrac{1 - \cos\left(\frac{\pi}{2}t\right)}{2} & \text{if } t < 2.0 \\ \hat{u}_f(0, y) & \text{otherwise} \end{cases} \quad ; \qquad \hat{u}_f(0, y) = 1.5\hat{u}_{\text{in}} \dfrac{y(H - y)}{\left(\frac{H}{2}\right)^2}$$

where $\hat{u}_{\text{in}} = 1$ is the average inflow velocity. For the solid domain, the bar of length 0.35 and thickness 0.02 is aligned to the center of the cylinder. The domain is meshed with 45k linear triangular elements in the fluid and 100 line elements on the solid, which are extruded to 200 bilinear quadrilateral elements. The problem is solved with a time step of $\delta t = 0.005$. For the boundary conditions, the bar is simply fixed at its left end. The Dirichlet transmission conditions are set on the fluid by imposing the solid velocity on the elements cut by the interface, while the Neumann transmission conditions are set by imposing the fluid tractions on the whole bar. The fluid density and viscosity are $\rho_f = 1000$ and $\mu_f = 1$, respectively, whereas the solid density, Young's modulus and Poisson's ratio are $\rho_s = 10^4$ $E_s = 1.4 \cdot 10^6$ and $\nu_s = 0.4$, respectively.

The results of the fluid domain are shown in Figs. 19 and 20 for velocity and pressure fields. For the solid domain, the original paper reports the time evolution of the displacement at the right end of the beam. At the fully developed state, when the oscillation's amplitude and frequency stabilize, the authors report displacements of -0.01458 ± 0.01244 and 0.00123 ± 0.0806, in the x-axis and
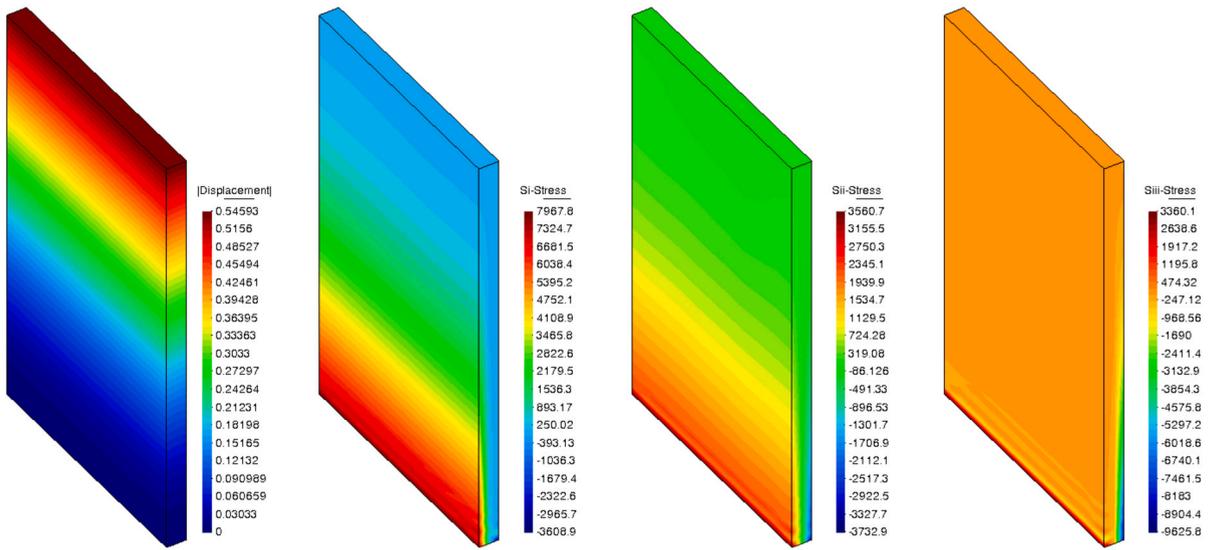
Fig. 17. 3D Vertical plate in a fluid tunnel - Displacement and PK2 principal stress fields.
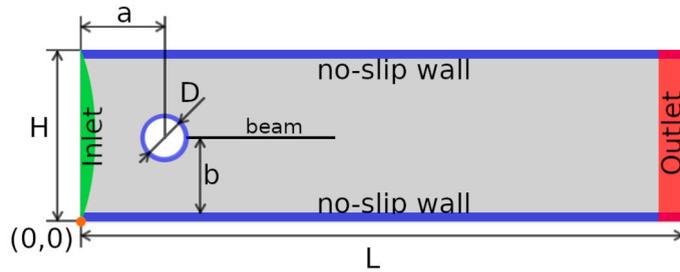

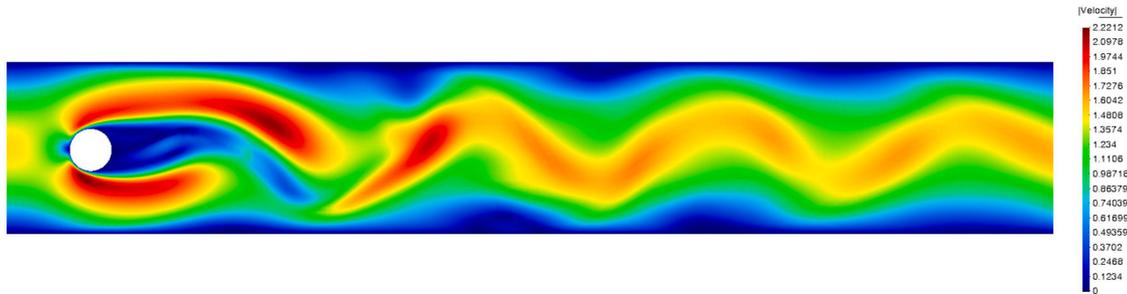**Fig. 18.** Turek benchmark - Geometry and boundary conditions.

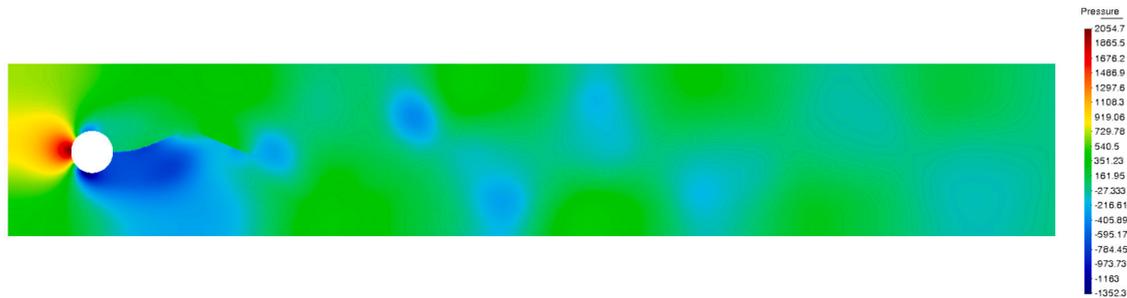**Fig. 19.** Turek benchmark - velocity norm at time $t = 7.61$.

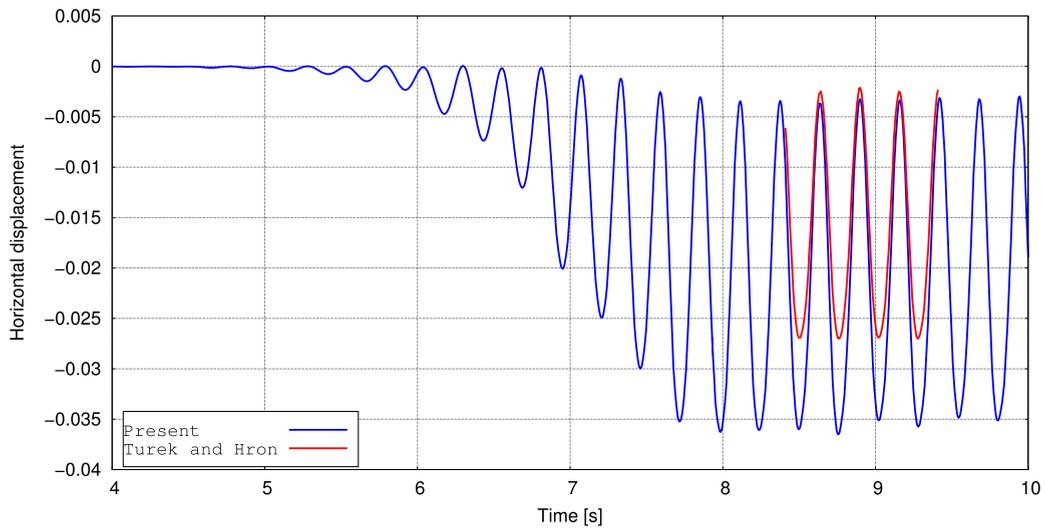**Fig. 20.** Turek benchmark - pressure at time $t = 7.61$.

Fig. 21. Turek benchmark - Horizontal displacement at the right end of the bar. Reference: Turek and Hron [67].
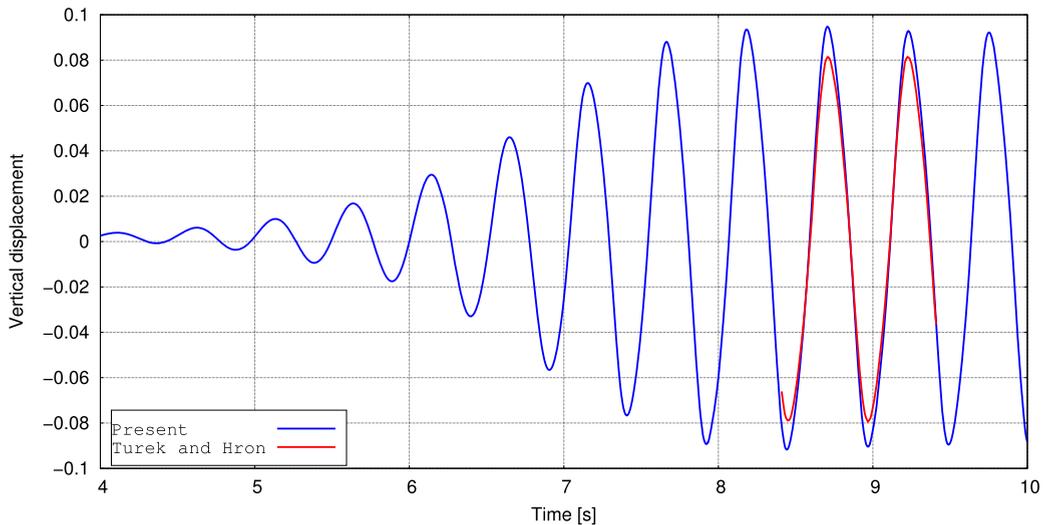

Fig. 22. Turek benchmark - Vertical displacement at the right end of the bar. Reference: Turek and Hron [67].

y-axis, respectively. They also provide a one second time span of the oscillations, which is used to compare our results in Figs. 21-22. The results obtained with our approach show good agreement when comparing the oscillation frequencies with respect to those in reference [67]. However, the amplitudes we have obtained are slightly larger, specially in the *x*-axis direction. As explained in Section 7, this can be attributed to several causes. Firstly, the material used in this work is a Neo-Hookean instead of the Saint-Venant–Kirchhoff material law used in the original paper. Secondly, the time step differs from those used in the original paper ($\delta t = 0.001, 0.002$). Lastly, and perhaps the most significant difference, in our approach the solid 'sees' the beam as a line, not as a rectangle. This in particular means that tractions are not integrated at the free end of the beam in the transverse direction, and they may be large enough to affect the physics of the solution.

9. Conclusion

In this work, a numerical framework for the approximation of FSI problems involving hyperelastic thin structures using an embedded approach is presented. The main novelty of this approach consists in approximating the solid domain by using a recently developed locking-free stabilized formulation for solid-shell elements [40,41]. The embedding of the solid mesh into the fluid mesh is not straightforward because solid-shell elements are thin volumetric bodies, which are not eligible to act as a embedding interface. For this reason, the issue is solved by using the solid-shell mid-surface as the interface to perform the embedding into the fluid domain. As a consequence, the transmission conditions of the Dirichlet-Neumann type require a special treatment.

This approach requires several key elements to function effectively. Firstly, from a computational standpoint, it is essential to implement a search algorithm to identify the background elements cut by the interface and an intersection algorithm to locate the intersections. This is achieved by utilizing a tree data structure that divides the domain into smaller sub-domains for the search and a ray-tracing algorithm to pinpoint the intersection points in each element. Secondly, from the fluid perspective, the embedded interface motivates the use of discontinuous shape functions to disconnect the pressures on each side of the interface. The fluid pressures are locally segregated at the element level, avoiding an increase in the computational overhead. The discontinuous shape functions are also suitable for weakly prescribing the Dirichlet transmission conditions using Nitsche's method, as they are imposed using the velocity of the embedded interface. Lastly, the Neumann transmission conditions are imposed by computing the fluid tractions at the embedded interface. Therefore, they need to be transferred to the solid-shell external surfaces.

The approach has undergone testing across various benchmark cases in both 2D and 3D environments, progressively increasing the difficulty in a staggered manner. Initially, one-way coupling cases have been addressed, testing the element-embedded interface and the weak imposition of boundary conditions on the fluid side. The evaluation has begun with a stationary problem, followed by a time-dependent problem featuring a periodic solution. Subsequently, a deformable solid has been introduced, and dynamic problems have been solved to assess the entire coupling scheme. The results have demonstrated good agreement with existing literature, establishing the presented framework as a viable method for approaching FSI problems with thin structures.

CRediT authorship contribution statement

A. Aguirre: Writing – review & editing, Writing – original draft, Software, Investigation. **R. Zorrilla:** Writing – review & editing, Writing – original draft, Investigation. **J. Baiges:** Writing – review & editing, Software, Investigation, Conceptualization. **R. Codina:** Writing – review & editing, Software, Investigation, Conceptualization.

Declaration of competing interest

None of the authors of the paper have a conflict of interest.

Acknowledgements

Data availability

All the information required for replicating the paper results was duly presented. Data files for the results are available upon request from the authors.

References

[1] P. Causin, J.-F. Gerbeau, F. Nobile, Added-mass effect in the design of partitioned algorithms for fluid–structure problems, Comput. Methods Appl. Mech. Eng. 194 (42–44) (2005) 4506–4527. Publisher: Elsevier.
[2] Y. Yu, H. Baek, G.E. Karniadakis, Generalized fictitious methods for fluid–structure interactions: analysis and simulations, J. Comput. Phys. 245 (2013) 317–346. Publisher: Elsevier.
[3] E.H. van Brummelen, Added mass effects of compressible and incompressible flows in fluid-structure interaction, J. Appl. Mech. 76 (2) (2009). Publisher: American Society of Mechanical Engineers Digital Collection.
[4] S.R. Idelsohn, F. Del Pin, R. Rossi, E. Oñate, Fluid–structure interaction problems with strong added-mass effect, Int. J. Numer. Methods Eng. 80 (10) (2009) 1261–1294. Publisher: Wiley Online Library.
[5] F. Nobile, Numerical approximation of fluid-structure interaction problems with application to haemodynamics, tech. rep., EPFL, 2001.
[6] P. Le Tallec, J. Mouro, Fluid structure interaction with large structural displacements, Comput. Methods Appl. Mech. Eng. 190 (24–25) (2001) 3039–3067. Publisher: Elsevier.
[7] M. Hirschhorn, V. Tchantchaleishvili, R. Stevens, J. Rossano, A. Throckmorton, Fluid–structure interaction modeling in cardiovascular medicine–a systematic review 2017–2019, Med. Eng. Phys. (2020). Publisher: Elsevier.
[8] M.S. Sacks, W.D. Merryman, D.E. Schmidt, On the biomechanics of heart valve function, J. Biomech. 42 (12) (2009) 1804–1824. Publisher: Elsevier.
[9] C. Farhat, K.G. Van der Zee, P. Geuzaine, Provably second-order time-accurate loosely-coupled solution algorithms for transient nonlinear computational aeroelasticity, Comput. Methods Appl. Mech. Eng. 195 (17–18) (2006) 1973–2001. Publisher: Elsevier.
[10] R. Kamakoti, W. Shyy, Fluid–structure interaction for aeroelastic applications, Prog. Aerosp. Sci. 40 (8) (2004) 535–558. Publisher: Elsevier.
[11] G.P. Guruswamy, A review of numerical fluids/structures interface methods for computations using high-fidelity equations, Comput. Struct. 80 (1) (2002) 31–41. Publisher: Elsevier.
[12] R. Loehner, C. Yang, J. Cerbal, J. Baum, H. Luo, D. Pelessone, C. Charman, Fluid-structure-thermal interaction using a loose coupling algorithm and adaptive unstructured grids, in: 29th AIAA, Fluid Dynamics Conference, 1998, p. 2419.
[13] W. Kim, H. Choi, Immersed boundary methods for fluid-structure interaction: a review, Int. J. Heat Fluid Flow 75 (2019) 301–309. Publisher: Elsevier.
[14] C.W. Hirt, A.A. Amsden, J. Cook, An arbitrary Lagrangian-Eulerian computing method for all flow speeds, J. Comput. Phys. 14 (3) (1974) 227–253. Publisher: Elsevier.

[15] T.E. Tezduyar, M. Behr, S. Mittal, J. Liou, A new strategy for finite element computations involving moving boundaries and interfaces-the deforming-spatial-domain/space-time procedure: II. Computation of free-surface flows, two-liquid flows, and flows with drifting cylinders, Comput. Methods Appl. Mech. Eng. 94 (3) (1992) 353–371. Publisher: Elsevier.

[16] C. Peskin, Flow patterns around heart valves: a digital computer method for solving the equations of motion, IEEE Trans. Biomed. Eng. 4 (1973) 316–317. Publisher: IEEE Computer Society.

[17] H. Udaykumar, W. Shyy, M. Rao, Elafint: a mixed Eulerian–Lagrangian method for fluid flows with complex and moving boundaries, Int. J. Numer. Methods Fluids 22 (8) (1996) 691–712. Publisher: Wiley Online Library.

[18] T. Dunne, An Eulerian approach to fluid–structure interaction and goal-oriented mesh adaptation, Int. J. Numer. Methods Fluids 51 (9–10) (2006) 1017–1039. Publisher: Wiley Online Library.

[19] D. Han, G. Liu, S. Abdallah, An Eulerian–Lagrangian–Lagrangian method for solving thin moving rigid body immersed in the fluid, Comput. Fluids 179 (2019) 687–701. Publisher: Elsevier.

[20] R.A.K. Sanches, H.B. Coda, On fluid–shell coupling using an arbitrary Lagrangian–Eulerian fluid solver coupled to a positional Lagrangian shell solver, Appl. Math. Model. 38 (July 2014) 3401–3418.

[21] T.J. Hughes, W.K. Liu, T.K. Zimmermann, Lagrangian-Eulerian finite element formulation for incompressible viscous flows, Comput. Methods Appl. Mech. Eng. 29 (3) (1981) 329–349. Publisher: Elsevier.

[22] F. Sotiropoulos, X. Yang, Immersed boundary methods for simulating fluid–structure interaction, Prog. Aerosp. Sci. 65 (2014) 1–21. Publisher: Elsevier.

[23] E. Fadlun, R. Verzicco, P. Orlandi, J. Mohd-Yusof, Combined immersed-boundary finite-difference methods for three-dimensional complex flow simulations, J. Comput. Phys. 161 (1) (2000) 35–60. Publisher: Citeseer.

[24] N.K.-R. Kevlahan, J.-M. Ghidaglia, Computation of turbulent flow past an array of cylinders using a spectral method with Brinkman penalization, Eur. J. Mech. B, Fluids 20 (3) (2001) 333–350. Publisher: Elsevier.

[25] M. Kirkpatrick, S. Armfield, J. Kent, A representation of curved boundaries for the solution of the Navier–Stokes equations on a staggered three-dimensional Cartesian grid, J. Comput. Phys. 184 (1) (2003) 1–36. Publisher: Elsevier.

[26] R.J. Leveque, Z. Li, The immersed interface method for elliptic equations with discontinuous coefficients and singular sources, SIAM J. Numer. Anal. 31 (4) (1994) 1019–1044. Publisher: SIAM.

[27] L. Ge, F. Sotiropoulos, A numerical method for solving the 3D unsteady incompressible Navier–Stokes equations in curvilinear domains with complex immersed boundaries, J. Comput. Phys. 225 (2) (2007) 1782–1809. Publisher: Elsevier.

[28] I. Babuška, The finite element method with penalty, Math. Comput. 27 (122) (1973) 221–228.

[29] K. Ito, K. Kunisch, Lagrange Multiplier Approach to Variational Problems and Applications, SIAM, Jan. 2008.

[30] J. Nitsche, Über ein Variationsprinzip zur Lösung von Dirichlet-Problemen bei Verwendung von Teilräumen, die keinen Randbedingungen unterworfen sind, Abh. Math. Semin. Univ. Hamb. 36 (July 1971) 9–15.

[31] P. Hansbo, Nitsche's method for interface problems in computational mechanics, GAMM-Mitt. 28 (2) (2005) 183–206, _eprint: https://onlinelibrary.wiley.com/doi/pdf/10.1002/gamm.201490018.

[32] G. Narváez, E. Schettini, J. Silvestrini, Numerical simulation of flow-induced vibration of two cylinders elastically mounted in tandem by immersed moving boundary method, Appl. Math. Model. 77 (Jan. 2020) 1331–1347.

[33] J. Ho, C. Farhat, Aerodynamic optimization with large shape and topology changes using a differentiable embedded boundary method, J. Comput. Phys. 488 (Sept. 2023) 112191.

[34] R. Nemer, A. Larcher, E. Hachem, Adaptive immersed mesh method (AIMM) for fluid–structure interaction, Comput. Fluids 277 (June 2024) 106285.

[35] S. Bailoor, A. Annangi, J.H. Seo, R. Bhardwaj, Fluid–structure interaction solver for compressible flows with applications to blast loading on thin elastic structures, Appl. Math. Model. 52 (Dec. 2017) 470–492.

[36] W.-Q. Wang, Y. Yan, G. Liu, An IB-LBM implementation for fluid-solid interactions with an MLS approximation for implicit coupling, Appl. Math. Model. 62 (Oct. 2018) 638–653.

[37] A. Hansbo, P. Hansbo, A finite element method for the simulation of strong and weak discontinuities in solid mechanics, Comput. Methods Appl. Mech. Eng. 193 (Aug. 2004) 3523–3540.

[38] E. Burman, S. Claus, P. Hansbo, M.G. Larson, A. Massing, CutFEM: discretizing geometry and partial differential equations, Int. J. Numer. Methods Eng. 104 (7) (2015) 472–501, _eprint: https://onlinelibrary.wiley.com/doi/pdf/10.1002/nme.4823.

[39] E. Burman, P. Hansbo, Fictitious domain finite element methods using cut elements: II. A stabilized Nitsche method, Appl. Numer. Math. 62 (Apr. 2012) 328–341.

[40] A. Aguirre, R. Codina, J. Baiges, Stress–displacement stabilized finite element analysis of thin structures using solid-shell elements, part I: on the need of interpolating the stresses, Finite Elem. Anal. Des. 236 (Sept. 2024) 104168.

[41] A. Aguirre, R. Codina, J. Baiges, I. Castañar, Stress–displacement stabilized finite element analysis of thin structures using solid-shell elements, part II: finite strain hyperelasticity, Finite Elem. Anal. Des. 236 (Sept. 2024) 104179.

[42] D. Boffi, F. Brezzi, M. Fortin, et al., Mixed Finite Element Methods and Applications, vol. 44, Springer, 2013.

[43] I. Castañar, J. Baiges, R. Codina, A stabilized mixed finite element approximation for incompressible finite strain solid dynamics using a total Lagrangian formulation, Comput. Methods Appl. Mech. Eng. 368 (Aug. 2020) 113164.

[44] I. Castañar, R. Codina, J. Baiges, A stabilized mixed three-field formulation for stress accurate analysis including the incompressible limit in finite strain solid dynamics, Int. J. Numer. Methods Eng. 124 (10) (2023) 2341–2366, tex.eprint: https://onlinelibrary.wiley.com/doi/pdf/10.1002/nme.7213.

[45] T.J. Hughes, G.R. Feijóo, L. Mazzei, J.-B. Quincy, The variational multiscale method - a paradigm for computational mechanics, Comput. Methods Appl. Mech. Eng. 166 (1–2) (1998) 3–24. Publisher: Elsevier.

[46] R. Codina, Stabilization of incompressibility and convection through orthogonal sub-scales in finite element methods, Comput. Methods Appl. Mech. Eng. 190 (2000) 1579–1599. Publisher: Elsevier.

[47] R. Codina, Finite element approximation of the three-field formulation of the Stokes problem using arbitrary interpolations, SIAM J. Numer. Anal. 47 (1) (2009) 699–718. Publisher: SIAM.

[48] S. Badia, R. Codina, Unified stabilized finite element formulations for the Stokes and the Darcy problems, SIAM J. Numer. Anal. 47 (Jan. 2009) 1971–2000. Publisher: Society for Industrial and Applied Mathematics.

[49] R. Codina, Stabilized finite element approximation of transient incompressible flows using orthogonal subscales, Comput. Methods Appl. Mech. Eng. 191 (39–40) (2002) 4295–4321. Publisher: Elsevier.

[50] S. Parada, J. Baiges, R. Codina, A fractional step method for computational aeroacoustics using weak imposition of Dirichlet boundary conditions, Comput. Fluids 197 (Jan. 2020) 104374. Publisher: Elsevier.

[51] E. Castillo, R. Codina, Finite element approximation of the viscoelastic flow problem: a non-residual based stabilized formulation, Comput. Fluids 142 (2017) 72–78. Publisher: Elsevier.

[52] L. Moreno, R. Codina, J. Baiges, E. Castillo, Logarithmic conformation reformulation in viscoelastic flow problems approximated by a VMS-type stabilized finite element formulation, Comput. Methods Appl. Mech. Eng. 354 (2019) 706–731. Publisher: Elsevier.

[53] R. Codina, S. Badia, J. Baiges, J. Principe, Variational multiscale methods in computational fluid dynamics, in: Encyclopedia of Computational Mechanics, second edition, John Wiley & Sons, Ltd, 2017, pp. 1–28, _eprint: https://onlinelibrary.wiley.com/doi/pdf/10.1002/9781119176817.ecm2117.

[54] R.F. Ausas, F.S. Sousa, G.C. Buscaglia, An improved finite element space for discontinuous pressures, Comput. Methods Appl. Mech. Eng. 199 (17–20) (2010) 1019–1031. Publisher: Elsevier.

[55] A.H. Coppola-Owen, R. Codina, Improving Eulerian two-phase flow finite element approximation with discontinuous gradient pressure shape functions, Int. J. Numer. Methods Fluids 49 (Dec. 2005) 1287–1304.

[56] R. Codina, J. Principe, J. Baiges, Subscales on the element boundaries in the variational two-scale finite element method, Comput. Methods Appl. Mech. Eng. 198 (2009) 838–852. Publisher: Elsevier.

[57] R. Codina, S. Badia, On the design of discontinuous Galerkin methods for elliptic problems based on hybrid formulations, Comput. Methods Appl. Mech. Eng. 263 (Aug. 2013) 158–168.

[58] S. Badia, R. Codina, T. Gudi, J. Guzmán, Error analysis of discontinuous Galerkin methods for the Stokes problem under minimal regularity, IMA J. Numer. Anal. 34 (Apr. 2014) 800–819, Conference Name: IMA Journal of Numerical Analysis.

[59] R. Zorrilla, A. Larese, R. Rossi, A modified finite element formulation for the imposition of the slip boundary condition over embedded volumeless geometries, Comput. Methods Appl. Mech. Eng. 353 (2019) 123–157. Publisher: Elsevier.

[60] R. Zorrilla, R. Rossi, R. Wüchner, E. Oñate, An embedded finite element framework for the resolution of strongly coupled fluid–structure interaction problems. Application to volumetric and membrane-like structures, Comput. Methods Appl. Mech. Eng. 368 (2020) 113179. Publisher: Elsevier.

[61] N. Delaissé, T. Demeester, R. Haelterman, J. Degroote, Quasi-Newton methods for partitioned simulation of fluid–structure interaction reviewed in the generalized Broyden framework, Arch. Comput. Methods Eng. 30 (June 2023) 3271–3300.

[62] S.R. Idelsohn, J.M. Gimenez, N.M. Nigro, Multifluid flows with weak and strong discontinuous interfaces using an elemental enriched space, Int. J. Numer. Methods Fluids 86 (12) (2018) 750–769. Publisher: Wiley Online Library.

[63] R. Zorrilla, A. Larese de Tetto, R. Rossi, A discontinuous Nitsche-based finite element formulation for the imposition of the Navier-slip condition over embedded volumeless geometries, Int. J. Numer. Methods Fluids 93 (9) (2021) 2968–3003. Publisher: Wiley Online Library.

[64] Z.-Q. Zhang, G.R. Liu, B.C. Khoo, Immersed smoothed finite element method for two dimensional fluid–structure interaction problems, Int. J. Numer. Methods Eng. 90 (10) (2012) 1292–1320, _eprint: https://onlinelibrary.wiley.com/doi/pdf/10.1002/nme.4299.

[65] D. Han, G. Liu, S. Abdallah, ELL for 3D FSI problems with thin flexible structures based on the continuum-based shell element, J. Fluids Struct. 103 (2021) 103281. Publisher: Elsevier.

[66] D. Han, G. Liu, S. Abdallah, An Eulerian-Lagrangian-Lagrangian method for 2D fluid-structure interaction problem with a thin flexible structure immersed in fluids, Comput. Struct. 228 (2020) 106179. Publisher: Elsevier.

[67] S. Turek, J. Hron, Proposal for numerical benchmarking of fluid-structure interaction between an elastic object and laminar incompressible flow, in: H.-J. Bungartz, M. Schäfer (Eds.), Fluid-Structure Interaction, in: Lecture Notes in Computational Science and Engineering, Springer, Berlin, Heidelberg, 2006, pp. 371–385.